

OSLO METROPOLITAN UNIVERSITY
STORBYUNIVERSITETET

Master's Degree in
Structural Engineering and Building Technology
Department of Civil Engineering and Energy Technology

MASTER THESIS

THESIS TITLE Two-way coupled fluid-structure interaction method on aerodynamic analysis of tall timber building using URANS	DATE 06 June 2021
	NUMBER OF PAGES 56
AUTHOR Koh Chuen Hon (Kandidatnr: 112) (Group 0008)	SUPERVISOR Dimitrios Kraniotis CO-SUPERVISORS Arnab Chaudhuri Haris Stamatopoulos

IN COLLABORATION WITH -	CONTACT PERSON -
-----------------------------------	----------------------------

SUMMARY
 The structural response of tall building to aerodynamic excitation can be simulated with the use of computational fluid dynamics (CFD) for wind flow and finite element method (FEM) for structural modelling. This study presents a two-way coupled fluid-structure interaction (FSI) method on aerodynamic analysis of a tall timber building using CFD-FEM co-simulation. To attain low computational cost, the flow is modelled in conjunction with unsteady Reynolds-Averaged Navier Stokes (URANS) equations and SST k- ω turbulence model. Tall timber building 'Mjøstårnet' is chosen as case study and modelled structurally by use of FEM. Aerodynamic behaviour of Mjøstårnet under different wind conditions is investigated.

3 KEYWORDS
fluid-structure interaction (FSI)
unsteady Reynolds-Averaged Navier-Stokes (URANS)
tall timber building

Preface

This master thesis is part of the two-year master's degree programme in Structural Engineering and Building Technology, carried out at the Department of Civil Engineering and Energy Technology, under the Faculty of Technology, Art and Design (TKD) at Oslo Metropolitan University (OsloMet) in Oslo.

I would like to express my gratitude to my supervisors, i.e. associate professor Dimitrios Kraniotis and associate professor Arnab Chaudhuri, both at the Department of Civil Engineering and Energy Technology, OsloMet, together with associate professor Haris Stamatopoulos from Department of Structural Engineering, Norwegian University of Science and Technology (NTNU). In addition, I would like to thank Rune Abrahamsen from Moelven for sharing the BIM of Mjøstårnet, and fellow student Vasileios Kotzamanis for his constructive feedbacks on this work.

Oslo, June 6th, 2021

Alex Koh

Abstract

The structural response of tall building to aerodynamic excitation can be simulated with the use of computational fluid dynamics (CFD) for wind flow and finite element method (FEM) for structural modelling. This study presents a two-way coupled fluid-structure interaction (FSI) method on aerodynamic analysis of a tall timber building using CFD-FEM co-simulation. To attain low computational cost, the flow is modelled in conjunction with unsteady Reynolds-Averaged Navier Stokes (URANS) equations and SST $k-\omega$ turbulence model. Tall timber building 'Mjøstårnet' is chosen as case study and modelled structurally by use of FEM. Aerodynamic behaviour of Mjøstårnet under different wind conditions is investigated. A two-time steps FSI method is proposed to resolve convergence issue on pressure field in CFD when time-varying velocity profile such as gust is imposed, without demanding excessive mesh refinement or smaller computational domain. This allows complex aerodynamic analysis using URANS.

Table of Content

1. Introduction.....	7
2. Methodology	10
2.1. Governing equations	10
2.2. Problem setup	12
2.3. Boundary conditions (BCs)	14
2.4. Finite element (FE) model of Mjøstårnet.....	18
2.5. Two-way coupled fluid-structure interaction (FSI).....	20
2.6. Cases.....	22
3. Results	24
3.1. Selecting boundary conditions model.....	24
3.2. Uncoupled test cases.....	27
3.3. FSI cases.....	30
4. Discussion	34
5. Summary and conclusion	36
References.....	37
Appendices	42
A. Effective terrain roughness y_0	42
B. BIM model of Mjøstårnet.....	43
C. Properties assigned in FE model	44
D. Preliminary testing on boundary conditions.....	47
E. Comparison between SKE and SSTKO models.....	51
F. Testing with ideal gas model	53
G. Animations	57

List of Figures

Figure 1 Mjøstårnet (a) site, (b) façade, and (c) wind rose based on 2019 wind data from Stavsberg Hamar station [20]	9
Figure 2 (a) computation domain and (b) mesh using Trimmed mesher for predominantly hexahedral cells	13
Figure 3 Mjøstårnet FE model (a) S4R shell (b) B31 beams, notation cross section in mm x mm and (c) CONN3D2 connector	13
Figure 4 Time-varying referenced velocity profile $u_h(t)$ for ECG shape	15
Figure 5 Overall workflow of FSI co-simulation	20
Figure 6 (a) uncoupled testing cases and (b) FSI cases	23
Figure 7 $u+$, $k+$, $\epsilon+$ and $\omega+$ profiles of inlet and outlet of CFD domain	25
Figure 8 C_p and P profiles of Mjøstårnet	26
Figure 9 C_p profile of Mjøstårnet under SSTKO model	26
Figure 10 (a) and (b) Velocity profile of selected probes, (c) maximum surface pressure at windward and leeward walls	27
Figure 11 (a) Velocity profile at selected probes under $\Delta t=0.1s$, (b) maximum surface pressure at windward and leeward walls at $\Delta t=0.1s$ and $\Delta t=0.01s$	28
Figure 12 (a) Velocity profile at selected probes, (b) maximum surface pressure at windward and leeward walls, comparison is made between pre- and post-processed data.	29
Figure 13 Relative displacements at rooftop and 11 th floor of the building under case 1	30
Figure 14 Total damping properties ξ of Mjøstårnet under different u_h and wind direction	31
Figure 15 Velocity at selected probes and maximum surface pressure under (a) case 2a, (b) case2b, and (c) case 3	32
Figure 16 Relative displacement at rooftop and 11th floor of Mjøstårnet under (a) Case 2a, (b) Case 2b and (c) Case 3	33
Figure 17 BIM of Mjøstårnet	43
Figure 18 Results of sensitivity study with different damping settings, with numerical solution of in 60s, based on (a) rooftop and (b) 11 th floor of the building	45
Figure 19 Mesh profile of (a) empty domain (b) domain with 6m cube (c) 6m cube	47
Figure 20 $U+$, $k+$, $\epsilon+$ and $\omega+$ profiles of (a) RN11-SKE, (b) RN11-SSTKO, (c) RN15-SKE, and (d) RN15-SSTKO	48
Figure 21 $\epsilon+$ profile using (a) RN11-SKE and (b) RN11-SSTKO, compared to if only slip wall applied to top boundary	49

Figure 22 C_p profile of 6m cube	49
Figure 23 C_p profile of 6m cube domain	50
Figure 24 μ_t/μ ratio profile of 6m cube domain	50
Figure 25 U^+ profile of 6m cube domain	50
Figure 26 μ_t/μ ratio profile	51
Figure 27 U^+ profile	52
Figure 28 C_p profile	52
Figure 29 Velocity profile at selected probes of flow domain	53
Figure 30 Pressure profile (maximum magnitude) at windward and leeward side of the walls	54
Figure 31 Selected velocity profile of flow domain at front and back of the building	54
Figure 32 Pressure profile (maximum magnitude) at windward and leeward side of the walls	55
Figure 33 Velocity profile at selected probes of flow domain under ECG shape time-varying wind, using ideal gas model	55
Figure 34 Pressure profile of selected probes and building surface under ECG shape time-varying wind, using ideal gas model	56

List of Tables

Table 1 Material properties for glulam GL30c and Norwegian Spruce	18
Table 2 Damping factors α_R and β_R assigned in FEM	19
Table 3 Davenport classification of effective terrain roughness	42
Table 4 Stiffness of connections of Mjøstårnet assigned in FEM	44
Table 5 Damping coefficient of connections of Mjøstårnet assigned in FEM	44
Table 6 Estimated δ and ξ	46

1. Introduction

Wind-induced action on tall buildings is a leading concern in the construction field, where aerodynamic response of structural system must be allowed for in the design stage to ensure their safety and serviceability. A number of methods are presented to assess the wind-induced actions, which can be grouped into wind tunnel test, computational wind engineering (CWE) and field measurement. Among them, CWE is a cost-effective way for aerodynamic analysis, however it is not yet widely used as conventional structural design tool [1], instead it is recognized in non-structural application such as pedestrian comfort and pollutant dispersion in urban environment. Nonetheless, CWE is increasingly utilized these days if backed by proper validation on their works.

CWE is a subfield of computational fluid dynamics (CFD). CFD allows analysis of fluid system with distinct stream of numerical solution techniques, e.g. finite volume method (FVM), a finite difference formulation which is used predominantly in commercial CFD codes. One crucial aspect in CWE is the modelling of atmosphere boundary layer (ABL) for wind generation, which is turbulence in nature. The underlying governing equations are based on Navier-Stokes (NS) equations, and three numerical approaches are commonly applied to capture the effects of turbulence [2]: turbulence models for Reynolds-averaged Navier-Stokes (RANS) equations, large eddy simulation (LES), and direct numerical simulation (DNS). RANS equations focus on the mean flow by time-averaging NS equations, and the effects of turbulence on mean flow are modelled. A wide-ranging of turbulence models have been developed and they are extensively used in industry due to low computations. For LES approach, mean flow and large eddies are solved, and the effect of unresolved small eddies are described by sub-grid scale (SGS) model. Compared to RANS equations, LES captures the anisotropic pattern of large eddies affected by boundary conditions (BCs), consequently increase computation requirement. Noted Hybrid LES/RANS technique such as Detached Eddy Simulation (DES) is available. The costliest method is the DNS approach, where mean flow and all turbulent fluctuations are solved with unsteady NS equations, exacting substantial small spatial grids and time steps in simulation.

With economical computations in the back of mind, turbulence model for RANS equations is favoured. Most of the ABL validation studies are based on steady RANS (SRANS) [3], and the same validated BCs are to be applied in this study using unsteady RANS (URANS). SRANS provides statistically steady description of turbulence model, whereas URANS with its time-derivative terms can be used for transient modelling. Solutions from URANS are able to produce unsteady fluctuation behind the building, although the flow does not give a clear spectral gap between its periodic motion and turbulence fluctuation [4]. By and large unsteady ABL modelling is imposed with time-independent BCs similar to that of steady flows, where inflow profiles remain the same throughout

simulation. The unsteady flow solution, in particular the vortex shedding around buildings, is then used for transient or quasi transient analysis. It is however appealing if time-dependent BCs such as gust is imposed. Simulation of gusts using URANS is not well established in ABL modelling, instead it has been widely tested on aerofoil structures. Heinrich and Reimer (2013) [5] have elaborated two approaches for gust modelling, i.e. disturbance velocity approach (DVA) and resolved gust approach (RGA). The DVA adds momentum source that represent gust onto the subject's surface directly and focuses on resulting forces on tested object but ignoring the flow around the object, while in RGA the gust is modelled at inlet boundary and the transport of the gust velocity will be instantaneous throughout the entire flow domain under incompressible model. The RGA method have been demonstrated by Länger-Möller (2018) [6] and Menegozzo et al. (2018) [7] on wind turbine under URANS simulation. To simulate a gust in this study, RGA method is adapted.

In structural engineering, finite element method (FEM) is the established tool for numerical solution of field problems which require determination of spatial distribution of one or more dependent variables. By harnessing CFD for wind flow and FEM for structural modelling, fluid-structural interaction (FSI) can be simulated to study aerodynamic responses of a building. Several FSI literatures can be found; Braun et al. (2009) [8] had presented aerodynamic and aeroelastic analyses on a tall building using LES, where the building is modelled as simple solid elastic body. Zhang et al. (2015) [9] used uncoupled FSI technique to predict wind-induced vibrations of high-rise buildings, applying DES to resolve wind flow once followed by parametric structural analysis. Similar study is performed by Wijesooriya et al. (2020) [10], where flow solution was extracted for implicit modal analysis. For non-building structures, FSI analysis has been applied on wind turbines [11, 12], offshore structures [13] and bridges [14, 15], as well as analysis of structure under fire and thermal loads [16, 17, 18, 19].

Tall timber buildings are scarce and consequently make the study on their dynamic behaviour challenging. It is therefore necessary to utilize simulation tools, and FSI co-simulation is a good candidate for studying their aerodynamic behaviour. Mjøstårnet located at Brumunddal, Norway is selected as the case study. Figure 1 shows the exterior of Mjøstårnet, site location and its wind rose. As of early 2021, Mjøstårnet is the highest building made structurally from timber with a height of 85.4m.

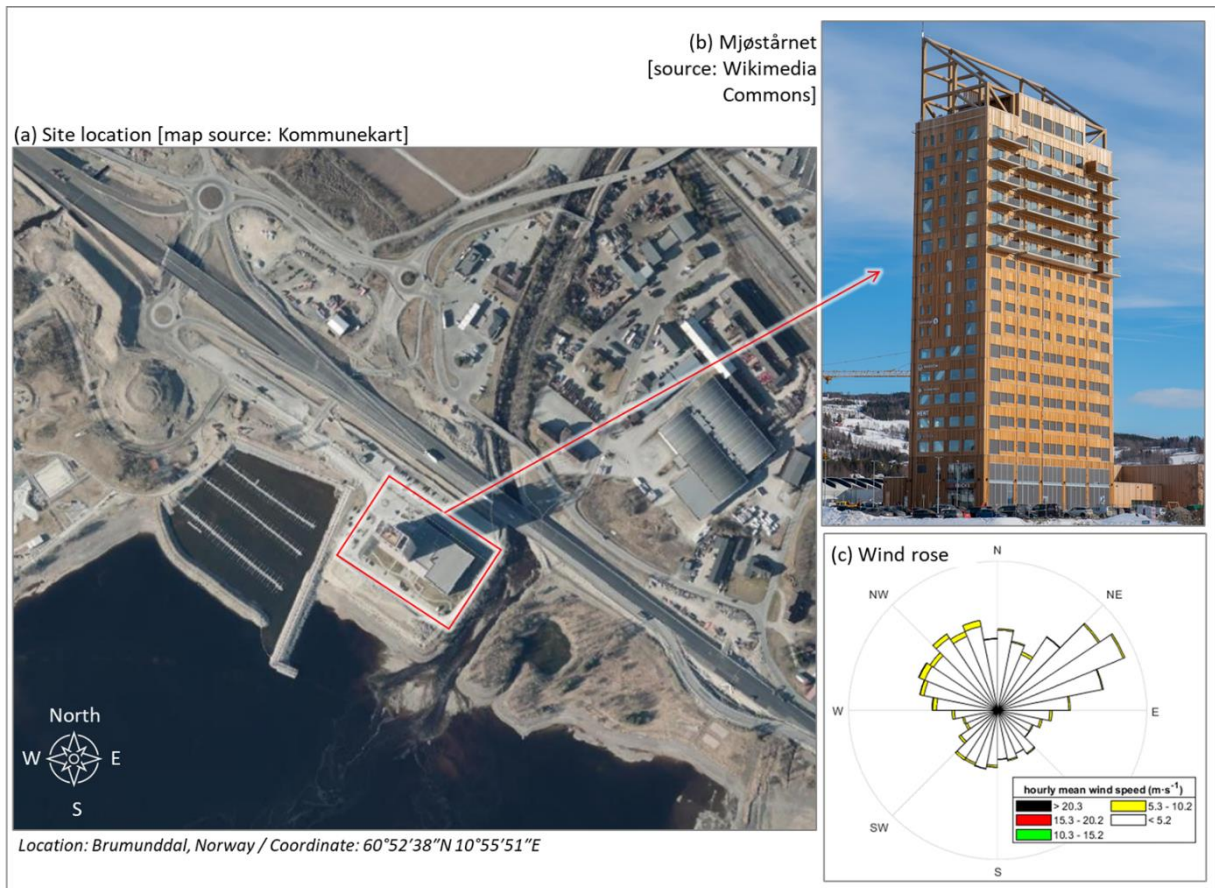


Figure 1 Mjøstårnet (a) site, (b) façade, and (c) wind rose based on 2019 wind data from Stavsberg Hamar station [20]

This study intends to explore the use of CFD-FEM co-simulation to investigate structural response of Mjøstårnet under service level aerodynamic loads without costly computations. The two-way coupled co-simulation involves two parts, i.e. wind flows are simulated with CFD commercial codes Star-CCM+ [21], and building is modelled and analysed using FEM commercial codes Abaqus [22]. ABL is simulated to generate incoming wind flow with RANS equations and turbulence model, with attention given to the setup of BCs. The structural components and their connections of Mjøstårnet are modelled based on the building information model (BIM) of Mjøstårnet received from producer (Moelven). Case studies are included to evaluate aerodynamic behaviour of Mjøstårnet under different wind conditions including gust.

2. Methodology

2.1. Governing equations

Aerodynamic flow around bluff body is turbulence in nature, and considered as incompressible owing to their relatively low speed [1]. In this study, Reynolds-averaged Navier-Stokes (RANS) equations for incompressible flow are used as the governing equations for the time-averaged properties of wind flow, which comprise of continuity equation Eq.(1) and time-average x -, y -, and z -momentum equations Eq.(2) [2]. Velocity vector \vec{u} is decomposed into mean \vec{U} and fluctuating \vec{u}' components, i.e. $\vec{u} = \vec{U} + \vec{u}'$ and its Cartesian components (mean U , V and W ; fluctuations u' , v' and w'). ρ and ν are constant density and viscosity of the flow, and P is the pressure field. Similarly, Eq.(3) is the general time-average transport equation of an arbitrary scalar quantity ϕ .

$$\nabla \cdot \vec{U} = 0 \quad (1)$$

$$\frac{\partial U}{\partial x} + \nabla \cdot (U\vec{U}) = -\frac{1}{\rho} \frac{\partial P}{\partial x} + \nu \nabla \cdot (\nabla U) + \frac{1}{\rho} \left[\frac{\partial(-\rho \overline{u'u'})}{\partial x} + \frac{\partial(-\rho \overline{v'u'})}{\partial y} + \frac{\partial(-\rho \overline{w'u'})}{\partial z} \right] \quad (2a)$$

$$\frac{\partial V}{\partial x} + \nabla \cdot (V\vec{U}) = -\frac{1}{\rho} \frac{\partial P}{\partial y} + \nu \nabla \cdot (\nabla V) + \frac{1}{\rho} \left[\frac{\partial(-\rho \overline{u'v'})}{\partial x} + \frac{\partial(-\rho \overline{v'v'})}{\partial y} + \frac{\partial(-\rho \overline{w'v'})}{\partial z} \right] \quad (2b)$$

$$\frac{\partial W}{\partial x} + \nabla \cdot (W\vec{U}) = -\frac{1}{\rho} \frac{\partial P}{\partial z} + \nu \nabla \cdot (\nabla W) + \frac{1}{\rho} \left[\frac{\partial(-\rho \overline{u'w'})}{\partial x} + \frac{\partial(-\rho \overline{v'w'})}{\partial y} + \frac{\partial(-\rho \overline{w'w'})}{\partial z} \right] \quad (2c)$$

$$\frac{\partial \phi}{\partial x} + \nabla \cdot (\phi \vec{U}) = \frac{1}{\rho} \nabla \cdot (\Gamma_\phi \nabla U) + \left[-\frac{\partial(\overline{u'\phi'})}{\partial x} - \frac{\partial(\overline{v'\phi'})}{\partial y} - \frac{\partial(\overline{w'\phi'})}{\partial z} \right] \quad (3)$$

Extra unknown terms appear from the time-averaging operation on the momentum and scalar transport equations and therefore additional turbulence model is required to close the RANS equations. Two turbulence models are included for testing in this study, i.e. standard k - ϵ (SKE) and Menter shear stress transport (SST) k - ω (SSKTO) turbulence models, both are eddy viscosity models with two additional transport equations. SKE turbulence model solves transport equation for turbulence kinetic energy k and turbulence dissipation rate ϵ in order to determine eddy viscosity μ_t , which is based on the model developed by Jones and Launder (1972) [23]. The SKE coefficients are obtained by Launder and Spalding (1974) [24], i.e.

$$\sigma_k = 1.0, \sigma_\epsilon = 1.3, C_{\epsilon 1} = 1.44, C_{\epsilon 2} = 1.92, C_\mu = 0.09$$

For SSKTO turbulence model, turbulence kinetic energy k and specific dissipation rate ω are solved instead, developed by Menter (1994) [25] with the intention to resolve free-stream conditions problem of standard Wilcox k - ω (SKO) model. In SSKTO model, SKE is used for far field while SKO for near wall by use of blending function. Standard SSKTO coefficients are applied, i.e.

$$a_1 = 0.31, \sigma_{k1} = 0.85, \sigma_{k2} = 1, \sigma_{\omega 1} = 0.5, \sigma_{\omega 2} = 0.856, \beta^* = 0.09, \beta_1 = 0.075, \beta_2 = 0.0828$$

For structural dynamics, the governing equation for finite elements can be expressed in Eq.(4) [26]. The nodal degree of freedom of structure \vec{D} is discrete functions of space but continuous functions of time. \vec{R}^{int} is internal stress vector and equivalent to $[K]\vec{D}$ for linearly elastic material, and \vec{R}^{ext} is externally applied forces to nodes. $[M]$, $[C]$ and $[K]$ are global mass, damping and stiffness matrices for a multi-element structure, respectively.

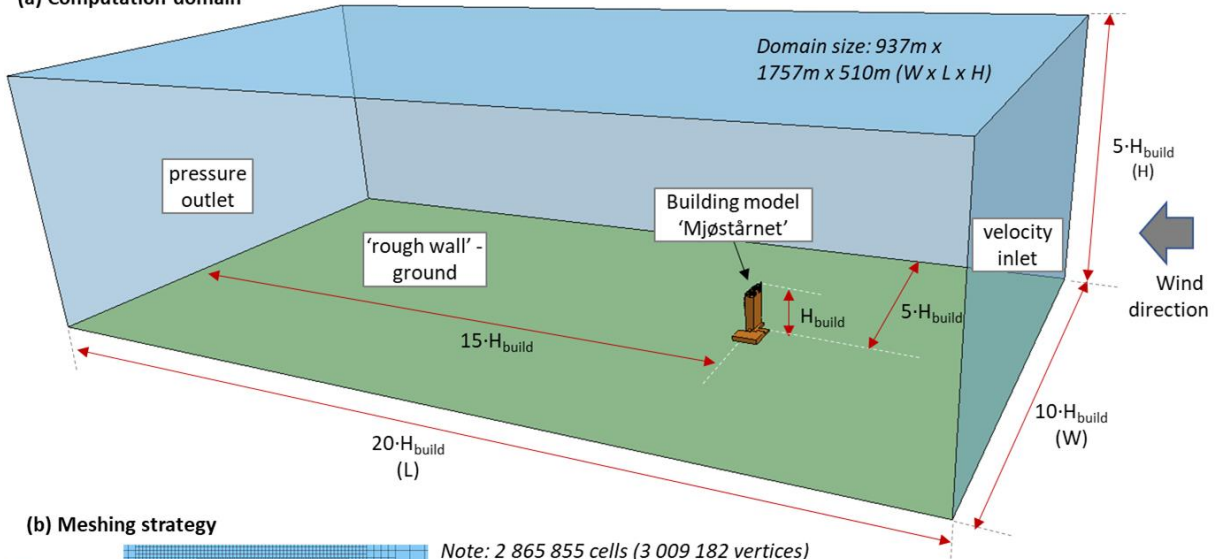
$$[M]\vec{\ddot{D}} + [C]\vec{\dot{D}} + \vec{R}^{int} = \vec{R}^{ext} \quad (4)$$

2.2. Problem setup

The CFD domain is setup based on assumption of a steady, incompressible, and horizontal homogeneous flow. For this reason, the ABL is assumed with constant air density ρ and viscosity μ . To account for flow with high Reynolds number [24], threshold for turbulence viscosity ratio μ_t/μ is set at 1×10^{10} . The size of computational domain is determined based on minimum distances between the building model and boundaries of the domain using building height H_{build} as base unit. The inflow, sides and upper boundaries should be at least $5 \cdot H_{build}$ from building model, and the outflow boundary should be at least $15 \cdot H_{build}$ away. The Mjøstårnet model has a maximum dimension at 87m x 57m x 85m ($W \times L \times H$) with main tower 37m x 17m x 85m ($W \times L \times H$), which gives $H_{build}=85$ m. The flow domain is then built based on minimum dimensional requirement, i.e. 937m x 1757m x 510m ($W \times L \times H$), shown in Figure 2a. Maximum allowable blockage ratio, i.e. ratio of building surface at windward side to cross-section of flow domain is 0.7%, which is well within the recommended 3% limit [3].

For Mjøstårnet, the structural components and their connections are modelled in FEM based on the BIM. Mjøstårnet consists of large-scale glulam trusswork of strength class GL30c according to EN14080 [27] as main load bearing along the facades and internal columns and beams [28]. CLT walls are used for secondary load bearing in elevators and staircases, however they are not included in the horizontal load-carrying system, therefore excluded from the model. All glulam elements are connected by use of slotted-in steel plates and dowels embedded deep into the timber for fire protection. Secondary elements including building envelope, balconies and attached buildings are modelled as timber wall elements for the purpose of coupling with fluid domain in CFD, by providing surfaces to take the wind loads. The dimension and properties of these secondary elements are only approximated. Three types of finite elements are applied in the building finite elements (FE) model (Figure 3), i.e. (i) B31: 2-node linear Timoshenko beam for all beams components, (ii) S4R: 4-node thin shell for floors and building envelope, and (iii) CONN3D2: 2-node connector elements.

(a) Computation domain



(b) Meshing strategy

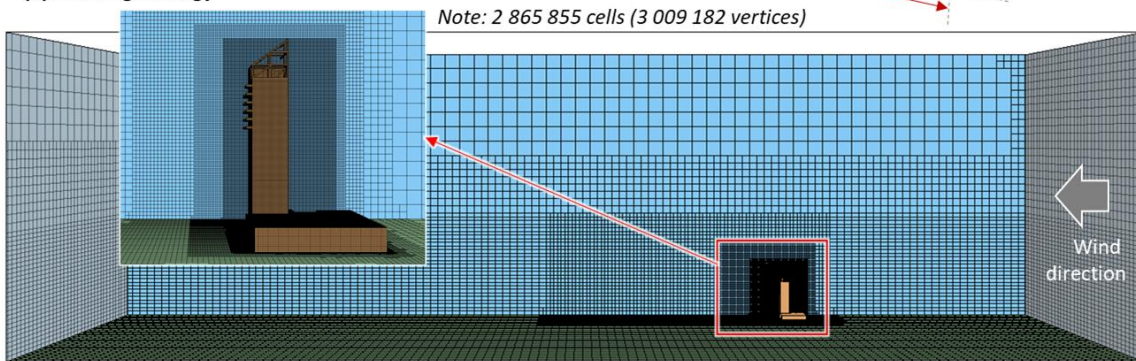


Figure 2 (a) computation domain and (b) mesh using Trimmed mesher for predominantly hexahedral cells

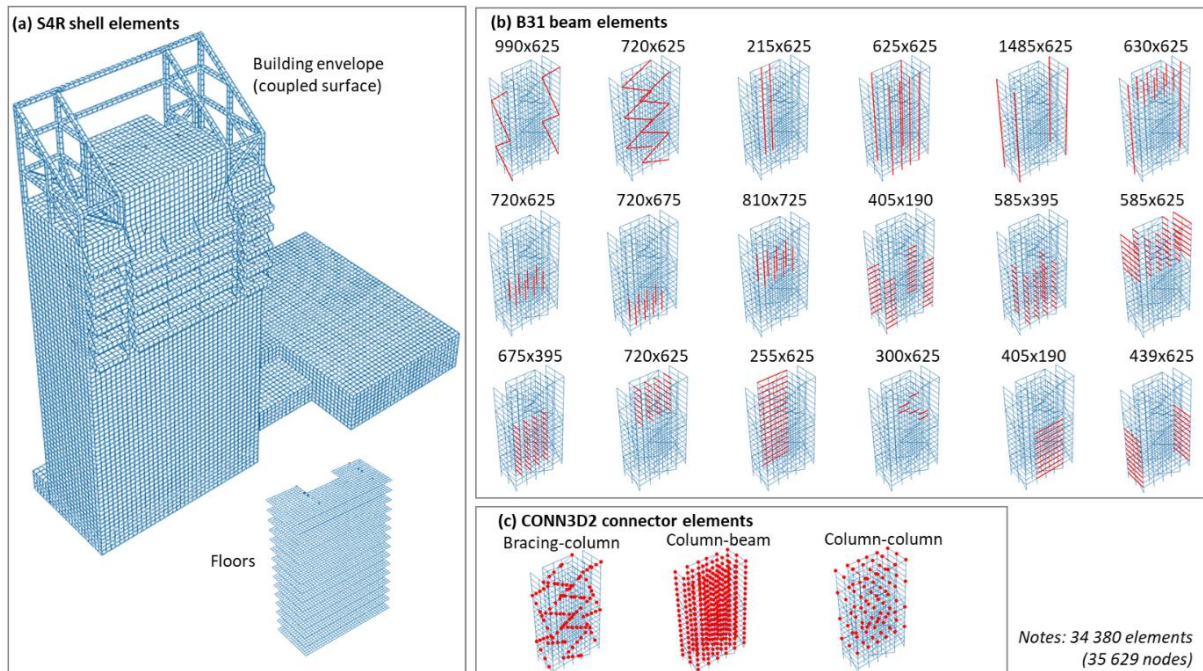


Figure 3 Mjøstårnet FE model (a) S4R shell (b) B31 beams, notation cross section in mm x mm and (c) CONN3D2 connector

2.3. Boundary conditions (BCs)

Based on SKE model, Richards and Hoxey (1993) [29] has introduced BC profiles of U , k and ε for a steady incompressible, two-dimensional flow of ABL, with dimensionless u^+ , k^+ and ε^+ expressed in Eq.(5), Eq.(6) and Eq.(7). Both u^+ and ε^+ profiles are height-dependent (distance y from ground) while k^+ is constant. The von Kármán's constant $\kappa=0.42\pm 0.01$ is applied, flow domain height H is used as the characteristic length of the geometry, and definition of effective terrain roughness y_0 is based on revised Davenport classification (2000) [30]. By rearranging Eq.(5) with referenced velocity $U(y) = u_h$ at reference height $y = h$, friction velocity u^* can be formulated into Eq.(8). The derived u^* is the central parameter for BCs formulation of ABL model, whereas referenced velocity u_h is used as main input for inflow profile.

$$u^+ = \frac{U(y)}{u^*} = \frac{1}{\kappa} \ln \left(\frac{y+y_0}{y_0} \right) \quad (5)$$

$$k^+ = \frac{k}{u^{*2}} = \frac{1}{\sqrt{C_\mu}} \quad (6)$$

$$\varepsilon^+ = \frac{\varepsilon(y) \cdot H}{u^{*3}} = \frac{H}{\kappa \cdot (y+y_0)} \quad (7)$$

$$u^* = \frac{\kappa \cdot u_h}{\ln \left(\frac{h+y_0}{y_0} \right)} \quad (8)$$

Richards and Norris (2011) [31] revisited the 1993 paper and incorporated additional turbulence models including SKO. The dimensionless ω^+ for SKO model is given in Eq.(9) with $\kappa=0.408$, whereas u^+ and k^+ profiles remain similar to SKE model. Similar equations can be applied for SSTKO model. For BCs of SKE model, adjustment on $\kappa=0.433$ is made from earlier work.

$$\omega^+ = \frac{\omega(y) \cdot H}{u^*} = \frac{\varepsilon}{\kappa \cdot \beta^*} \cdot \frac{H}{u^*} = \frac{H}{\kappa \cdot \sqrt{\beta^*} \cdot (y+y_0)} \quad (9)$$

The BCs above are modelled as horizontally homogeneous atmospheric surface layer, and the flow is driven by a constant shear stress throughout the ABL. This requires a constant shear stress at top BC. As an alternative, Richards and Norris (2015) have derived BCs for an equilibrium pressure driven boundary layer [32], which provides a reasonable model for lower half of ABL where shear stress decreases linearly with height. This model can be used in conjunction with a free-slip top BC, which is commonly applied in practice. Both SKE and SSTKO models are included with fitting polynomial equations for u^+ , k^+ , ε^+ and ω^+ , i.e. Eq.(10a), Eq.(11a) and Eq.(12) for SKE model, and Eq.(10b), Eq.(11b) and Eq.(13) for SSTKO model, by fixing $\kappa=0.4$. In these models, k^+ has been transformed into a height-dependant profile. In addition, H is set as half of the gradient height h_g as per Eq.(14a). Notation $Y = (y + y_0)/H$ is used below. Noted domain height H in this study is designed at $5 \cdot H_{build}$. Eq.(14a) necessitates H to be proportional to u^* , however this will increase the domain size under higher u_h or rougher y_0 . A compromised approach where $H = 5 \cdot H_{build}$ is applied

for the flow domain dimension, and to account for low u_h , Eq.(14a) is modified into Eq.(14b) to be used in conjunction with Eq.(10) to Eq.(13)

$$u_{k\varepsilon}^+ = \frac{U(y)}{u^*} = 2.5 \left(\ln \left(\frac{y+y_0}{y_0} \right) + 0.528 \cdot Y + 0.385 \cdot Y^2 - 1.090 \cdot Y^3 + 0.243 \cdot Y^4 \right) \quad (10a)$$

$$u_{k\omega}^+ = \frac{U(y)}{u^*} = 2.5 \left(\ln \left(\frac{y+y_0}{y_0} \right) + 0.280 \cdot Y - 0.331 \cdot Y^2 - 0.334 \cdot Y^3 + 0.096 \cdot Y^4 \right) \quad (10b)$$

$$k_{k\varepsilon}^+ = \frac{k(y)}{u^{*2}} = 0.921 + 3.533(1 - Y)^2 - 1.926(1 - Y)^4 + 0.805(1 - Y)^6 \quad (11a)$$

$$k_{k\omega}^+ = \frac{k(y)}{u^{*2}} = 1.056 + 2.814(1 - Y)^2 - 0.834(1 - Y)^4 + 0.297(1 - Y)^6 \quad (11b)$$

$$\varepsilon^+ = \frac{\varepsilon(y) \cdot H}{u^{*3}} = \frac{0.225 \cdot k^{+2}}{Y} (1 + 1.528(Y) + 2.298(Y)^2 - 0.972(Y)^3) \quad (12)$$

$$\omega^+ = \frac{\omega(y) \cdot H}{u^*} = \frac{2.5 \cdot k^+}{Y} (1 + 1.280(Y) + 0.618(Y)^2 - 0.384(Y)^3) \quad (13)$$

$$H \approx \frac{h_g}{2} \approx 809 \cdot u^* \quad (14a)$$

$$H = \max (5 \cdot H_{build} , 809 \cdot u^*) \quad (14b)$$

To simulate a gust in this study, RGA method is loosely adapted to the u^+ (Figure 4) by applying unsteady $u_h(t)$ profile using Eq.(15), based on the Extreme Coherent Gust (ECG) shape from IEC standard [33]. Parameters include gust amplitude u_g , time with peak gust t_{pg} , peak gust duration Δt_g , gust period T_g , t_i is when the ECG starts, and referenced mean velocity $u_{h,0}$.

$$u_h(t) = \begin{cases} u_{h,0} & , t < t_i \text{ and } t > t_i + T_g \\ u_{h,0} + 0.5 \cdot u_g \cdot \left(1 + \cos \left(2\pi \cdot \frac{t-t_{pg}}{T_g - \Delta t_g} \right) \right) & , t_i \leq t \leq t_{pg} \\ u_{h,0} + u_g & , t_{pg} < t < t_{pg} + \Delta t_g \\ u_{h,0} + 0.5 \cdot u_g \cdot \left(1 + \cos \left(2\pi \cdot \frac{t-t_{pg}-\Delta t_g}{T_g - \Delta t_g} \right) \right) & , t_{pg} + \Delta t_g \leq t \leq t_i + T_g \end{cases} \quad (15)$$

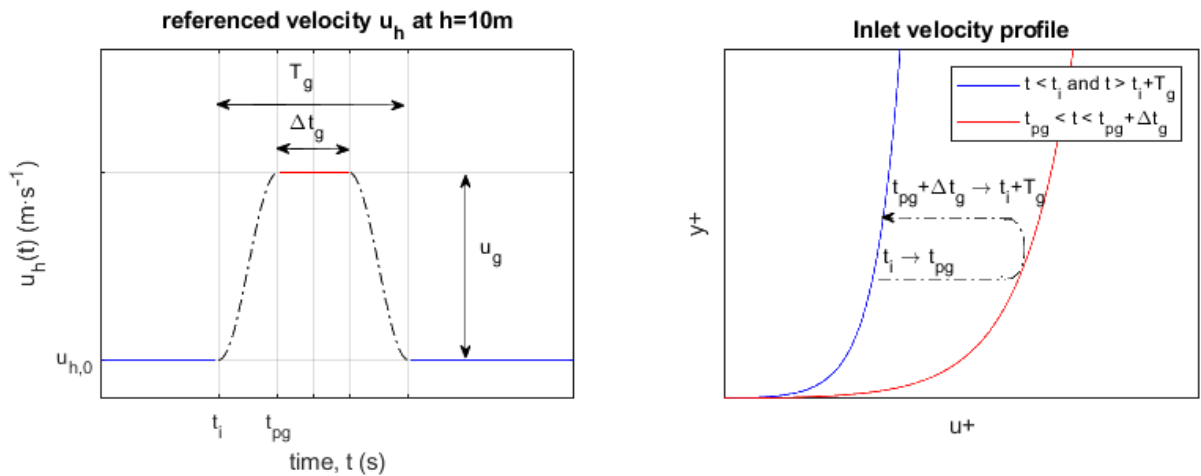


Figure 4 Time-varying referenced velocity profile $u_h(t)$ for ECG shape

The surrounded terrain for Mjøstårnet is assumed as ‘roughly open’ with $y_0=0.10$ [30]. For the first cell layer nearest to the bottom of computational domain, wall function is applied to model y_0 , and equivalent sand-grain roughness height r is used as wall surface parameter [21]. Blocken et al. (2007) [34] has provided a comprehensive study on wall function problems in ABL simulation including relationship between r and y_0 . In theory, the inner turbulent boundary layer can be divided into three sublayers, i.e. viscous sublayer next to the wall which is dominated by viscous effect, log layer next to the outer boundary layer which is dominated equally by viscous and turbulence effects, and buffer layer in between them. These sublayers are modelled using different empirical approaches, generally expressed in dimensionless wall distance y^+ in Eq.(16) and u^+ . It is hence critical to model the first cell layer thickness correctly to the desired sublayer, i.e. log layer $y^+ \geq 30$. Eq.(17) is used in this study to model the terrain roughness by adjusting the log layer relative to the wall. Coefficient $C^*=0.253$ and $E^*=9.0$ are used, and κ depends on the applied turbulence model. By comparing Eq.(17) to Eq.(5), a relationship between r and y_0 can be formulated as Eq.(18).

$$y^+ = \frac{y \cdot \rho \cdot u^*}{\mu} \quad (16)$$

$$u^+ = \frac{1}{\kappa} \ln \left(\frac{E^*}{C^*} \cdot \frac{y}{r} \right) \quad (17)$$

$$r = \frac{E^*}{C^*} y_0 = 35.6 y_0 \quad (18)$$

Three considerations need to be taken into account when deciding the lower near wall cells [34, 35], (i) sufficiently high mesh resolution, (ii) centroid of near wall cell y_p is larger than r , i.e. $y_p > r$, and (iii) wall distance $y^+ > 30$ to ensure the cells are in the log layers. Using these criteria, the thickness of near wall cell for ground $y_{g1}=7.12\text{m}$ is applied in the computational domain.

To avert turbulence decay in flow domain under shear-driven models, the flow has to be driven by a constant shear stress across the boundary [29, 36]. It is therefore required to apply a constant shear stress τ throughout the boundary layer, and the top BC should be treated with constant τ , zero flux k , and constant flux of ε and ω [31]. O’Sullivan et al. (2011) [37] has imposed Neumann BC at the top with fixed gradient condition as described in Eq.(19) and (20), in conjunction with Eq.(5) to Eq.(7). By using the same procedure, Eq.(21) is derived for SSTKO model. Richard and Norris (2011) [31] proposed to create a thin layer of sub-domain at top boundary to prescribe constant τ and ε gradient to drive the flow, if it is difficult to apply the BC directly. Other solution with Dirichelet BC such as creating a secondary velocity inlet at top boundary with fixed u , k , ε and ω , where direction of u is parallel to the top boundary following the flow direction is proposed by Zhang (2009) [38]. Blocken et al. (2007) [34] has fixed the u , k and ε values for the top cells using same values from inlet profile at top height.

$$\frac{\partial u}{\partial y} = \frac{u^*}{\kappa \cdot (y+y_0)} \quad (19)$$

$$\frac{\partial \varepsilon}{\partial y} = \frac{-u^{*3}}{\kappa \cdot (y+y_0)^2} \quad (20)$$

$$\frac{\partial \omega}{\partial y} = \frac{-u^*}{\kappa \cdot \sqrt{\beta^*} \cdot (y+y_0)^2} \quad (21)$$

To recap, the computational domain is set up with following BCs:

- i. Upstream BC: Velocity inlet is applied; four inflow BC models are included for testing, i.e. Richards and Norris (2011) SKE and SSTKO models (“RN11-SKE” and “RN11-SSTKO”), and Richards and Norris (2015) SKE and SSTKO models (“RN15-SKE” and “RN15-SSTKO”).
- ii. Lower BC: No-slip wall condition is applied for both terrain and building model; terrain is modelled with rough wall function using Eq.(18); building is modelled as smooth. High- y^+ wall treatment is applied due to $y^+ > 30$ setting.
- iii. Upper BC: Velocity inlet is imposed when applying RN11-SKE and RN11-SSTKO models with constant k and gradient for u , ε and ω profiles using Eq.(19), Eq.(20) and Eq.(21). For RN15-SKE and RN15-SSTKO model, only free-slip top BC is applied.
- iv. Downstream BC: Pressure outlet is applied with zero working pressure and similar k^+ , ε^+ and ω^+ profiles to upstream BC.
- v. Side BC: Symmetry plane is applied, where normal velocity and gradient of all turbulence quantities are zero.

2.4. Finite element (FE) model of Mjøstårnet

The material properties used in the FE model are summarized in Table 1. In this study, all timber elements are modelled as transversely isotropic. For glulam, the material properties are obtained from EN14080 [27] for GL30c class. There are two types of floors in Mjøstårnet, i.e. concrete floors at upper stories and timber composite lower floors [28]. The composite timber floors were approximately modelled by orthotropic shell elements with equivalent properties to Norwegian Spruce, which were calibrated such that the stiffness of the floors is represented with an equivalent thickness 150mm. The concrete floors are modelled as isotropic shell elements with thickness 300mm and material properties according to Table 1. To evaluate the response in this study, the floor mass was derived from quasi-permanent loads according to EN1990 [39], i.e. $G_k + \psi_2 \cdot Q_k$, where $G_k=2 \text{ kN}\cdot\text{m}^{-2}$, $Q_k=2 \text{ kN}\cdot\text{m}^{-2}$ for residential use and $3 \text{ kN}\cdot\text{m}^{-2}$ for offices [40] and $\psi_2=0.3$ according to EN1990 [39]. For coupling with CFD, building envelope and secondary elements such as balconies are included to provide surface areas for traction (Figure 3a). The building envelop is modelled by 50mm-thick shell elements and are tie-constrained to the main glulam structures.

Table 1 Material properties for FE model

Type	Density ρ ($\text{kg}\cdot\text{m}^{-3}$)	Elasticity modulus E ($\times 10^6 \text{ N}\cdot\text{m}^{-2}$)	Shear modulus G ($\times 10^6 \text{ N}\cdot\text{m}^{-2}$)	Poisson's ratio ν (-)
GL30c	430	$E_0=13000, E_{90}=300$	$G_0=650, G_{90}=65$	-
Norwegian spruce	470	$E_0=13000, E_{90}=410$	$G_0=760, G_{90}=30$	-
Concrete floor	2350	$E=25100$	-	0.15

All glulam connections are modelled as semi-rigid joints using CONN3D2 elements. Only viscoelasticity property is applied by having linear elastic springs and viscous dampers arranged in parallel, representing delayed-elastic or recoverable creep component of the dynamic response [41]. The translational stiffness $K_{ser,d}$ of the connections was obtained by use of EN1995-1-1 [42] with Eq.(22) and Eq.(23), where K_{ser} is slip modulus, n_{sp} is number of shear plane in connection, ρ is density of timber member and d_c is diameter of bolt. The rotational stiffness $K_{ser,\theta}$ of the connections was also taken into account in the model according to Eq.(24) [43], where $x_{c,i}$ and $y_{c,i}$ are the coordinates of bolts relative to the centroid of connection.

$$K_{ser} = 2 \cdot n_{sp} \cdot \rho^{1.5} \cdot d_c / 23 \quad (22)$$

$$K_{ser,d} = n_{dowel} \cdot K_{ser} \quad (23)$$

$$K_{ser,\theta} = K_{ser} \cdot \sum_{i=1}^n (x_{c,i}^2 + y_{c,i}^2) \quad (24)$$

The eigenfrequencies of the building and the corresponding mode shapes were obtained by modal analysis of the FE model. According to the modal analysis the fundamental eigenfrequency for translational mode of vibration is 0.89Hz, which is notably higher than the approximate first eigenfrequency at 0.35Hz [28] in the original model of Mjøstårnet. For reference, value from 0.33Hz to 0.75Hz can be found on other existing tall timber buildings [44, 45].

Rayleigh damping was assumed using Eq.(25a) [22] with parameters α_R and β_R for mass and stiffness proportional damping factors. For CONN3D2 elements, by assuming only stiffness proportional damping contributes, Eq.(25a) is reduced to Eq.(25b). The damping property of glulam beams is adopted from experimental works on GL32c by Labonnote et al. (2013) [46, 47], i.e. damping ratio $\xi=1.13\%$. For Norwegian spruce, $\xi=0.64\%$ is taken from the same study [46, 47] with solid wood C24 samples. Recommended ξ given in ISO 10137 [48] is taken to approximate timber composite floor and concrete floor, i.e. 2% for wood joist floor and 1.3% for simply supported concrete slab. For glulam truss with slotted in steel plates and dowels, assessment by Landel et al. (2018) [49] suggested $\xi=1.67\%$ at first mode, while another earlier study by Reynolds et al. (2012) [50] indicates ξ to be around 1.6% to 2.3%. In this study, $\xi=1.9\%$ is used for all connections. Precise modelling of soil-structure interaction is not included, and the damping contribution from the soil-structure interaction is only modelled using Eq.(25a) by assuming any vibrations will be damped via the connection between columns and foundations. The damping properties used in this study are summarized in Table 2.

$$C = \alpha_R \cdot M + \beta_R \cdot K \quad (25a)$$

$$C = \xi \frac{2}{(\omega_n)} \cdot K \quad (25b)$$

Table 2 Damping properties assigned in FE model

Sr. No.	ξ (%)	α_R (s ⁻¹)	β_R (s)
Glulam	1.13	0.04539	0.002588
Norwegian spruce	0.64	0.02571	0.001466
Concrete floor	1.30	0.05222	0.002977
Timber composite floor	2.00	0.08034	0.004580
Connection	1.90	-	-

The structural damping ratio ξ_s of Mjøstårnet FE model is around 1.2%, which is lower than 1.9% used in the design of Mjøstårnet [28] and another tall timber building Treet [51]. For comparison, $\xi=0.64\%$ to 9% are reported in other timber buildings including hybrid timber constructions [44, 45].

2.5. Two-way coupled fluid-structure interaction (FSI)

In two-way coupled FSI method, CFD exports wind loads in wall shear stress τ and pressure P to FEM, and FEM exports structural response in displacements d back to CFD. Within FEM, the wind loads are applied to the building's shell surface; while in CFD, the displacements are used to update the building's boundary in the flow domain. The specified field data are traded across a shared interface with a set of coupled boundaries. Surface-to-surface data mapping is used in this study, and for seamless interfacing, Mjøstårnet FE model is converted into CAD model and exported to CFD, which is then used to map with the original FE model. The FSI basic workflow is illustrated in Figure 5.

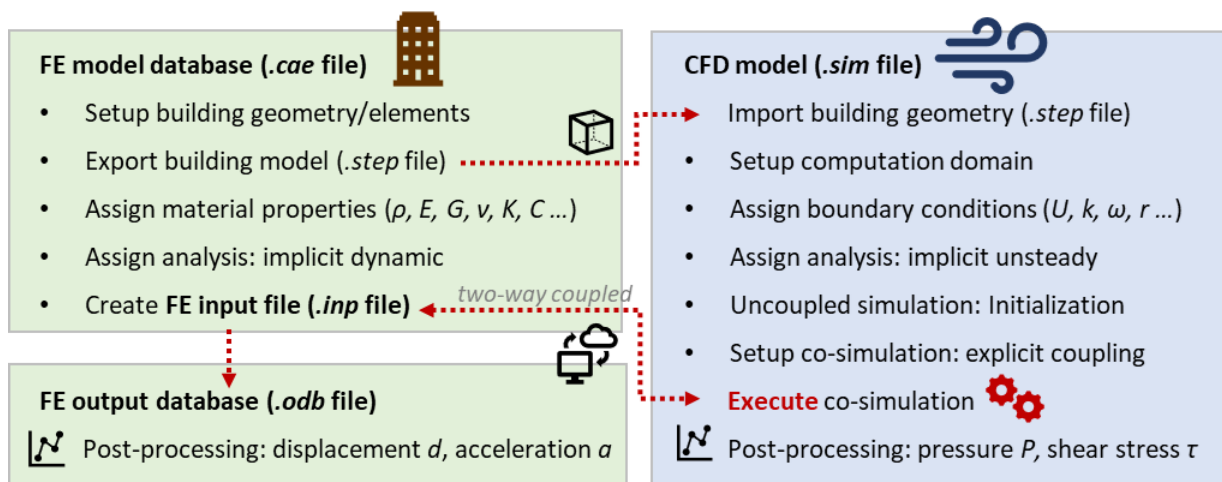


Figure 5 Overall workflow of FSI co-simulation

Mesh motion in CFD, or known as morphing for non-rigid deformation, allows positions of the initial mesh vertices to move in response to the displacement of the coupled surface boundaries. The morphing is done by redistributing the mesh vertices in response to the displacement at the interfaced boundaries without changing the number of cells. Interpolation algorithms, e.g. radial basis function (RBF) is used to calculate the displacement vector and use them to translate the mesh vertices to their new positions. The boundary vertices at the mapped surface (i.e. building) are displaced per time-step relative to initial mesh position. The vertices of the ground boundary are fixed in space and provide control points for use in calculating the interpolation field, while other are simply constrained.

Implicit URANS using segregated flow solver is implemented in CFD. The solver is based on discretized second order upwind scheme for convection flux, and second order temporal discretization accuracy scheme. For flow initialization, the physical time required for the wind flow to fully develop in the whole domain is dependent on the domain length L and u_h . For instant, 150-200s is required for $u_h = 11.1\text{m}\cdot\text{s}^{-1}$, 100s for $u_h = 22\text{m}\cdot\text{s}^{-1}$, and up to 1000s for $u_h = 2\text{m}\cdot\text{s}^{-1}$.

Implicit dynamic using Hilber-Hughes-Taylor (HHT) time integration solver is used as the FE solver for the dynamic analysis. The HHT method (also known as α -method) is an extension to the classic Newmark method (β -method), where parameter α introduces numerical damping in its procedure [52]. Decreasing α will provide additional numerical damping, while $\alpha=0$ reduce α -method to β -method with no damping introduced. Two α values are recommended, i.e. $\alpha=-0.05$ for minimum dissipation and $\alpha=-0.41421$ for moderate dissipation [22]. In this study, $\alpha=-0.05$ is applied, however if solution has difficulty to converge, $\alpha=-0.41421$ is used instead. Non-linear analysis is included to account for geometric nonlinearity, though it is not essential in the FSI analysis here.

The FSI models are first initialized with URANS until flow solution are converged. Once a converged flow solution is obtained, the flow solver is then coupled with FE solver for co-simulations. Explicit coupling scheme is applied for co-simulation where structure and fluid are weakly coupled and exchange data as per defined time-step. To resolve dynamic behaviour of building structure such as vibration, the time step should be smaller than the expected period of natural frequency of structure to capture any change in responses. Co-simulation time steps is consequently based on FE analysis requirement, where FEM will 'lead' the CFD in the time marching sequence. Minimum 1×10^{-6} s and maximum 0.1s time step are applied for the full simulation period. In this co-simulation, Star-CCM+ is used as main interface for execution, and Abaqus input (*.inp) file is used as FEM source code for the co-simulation. Normalized residuals of momentum, transport and continuity equations are used to control the inner iteration within CFD, which is set at 1×10^{-3} or lower and capped at maximum 20 inner iterations for each time step.

2.6. Cases

Mjøstårnet is located at Brumunddal Norway, therefore wind data from nearby Stavsberg Hamar weather station is make use of [20]. Maximum mean wind $11.1\text{m}\cdot\text{s}^{-1}$ at $h=10\text{m}$ is used as referenced wind u_h . The fundamental value of basic wind velocity $u_{b,o}=22\text{m}\cdot\text{s}^{-1}$ for Brumunddal [53] is also included to represent strong wind condition which is close to the recorded maximum hourly wind gust at $21.6\text{m}\cdot\text{s}^{-1}$ [20]. The dominant wind direction is from north-eastern (N.E.) (Figure 1b), i.e. ‘back’ side of Mjøstårnet should be facing to the upstream direction.

The BC models (RN11-SKE, RN11-SSTKO, RN15-SKE and RN15-SSTKO) are first tested on the CFD domain with SRANS. Inflows with $u_h=11.1\text{m}\cdot\text{s}^{-1}$ N.E. wind is checked first, followed by $u_h=22\text{m}\cdot\text{s}^{-1}$ south-western (S.W.), north-western (N.W.) and south-eastern (S.E.) wind for substantiating the testing. Conservation of u , k , ε and ω profiles at inlet and outlet are examined, together with building C_p profiles. One BC model is to be selected in the end of this exercise.

Three uncoupled test cases (Figure 6a) are included. Test 1 is based on time-independent inflow boundary profile, i.e. constant $u_h=11.1\text{m}\cdot\text{s}^{-1}$ and $22\text{m}\cdot\text{s}^{-1}$. The unsteady fluctuation patterns generated by the BCs, velocity and pressure profiles at selected points are extracted for study. For Test 2, a simple discrete change of u_h from $22.0\text{m}\cdot\text{s}^{-1}$ to $22.1\text{m}\cdot\text{s}^{-1}$ is applied in a single time step. Pressure profile during the change of inflow velocity is examined. Last, an ECG profile with $T_g=5\text{s}$, $u_g=5\text{m}\cdot\text{s}^{-1}$ and $\Delta t_g=0\text{s}$ is used to investigate the feasibility of applying time-varying inflow profile.

Three wind flow scenarios (Figure 6b) are included in the FSI aerodynamic analysis of Mjøstårnet, i.e. constant u_h , ECG u_h profile, and partial coupled ECG u_h profile. Under constant u_h scenario (case 1), $u_h=2\text{m}\cdot\text{s}^{-1}$, $11.1\text{m}\cdot\text{s}^{-1}$, $16\text{m}\cdot\text{s}^{-1}$, and $22\text{m}\cdot\text{s}^{-1}$ with N.E., S.W., N.W. and S.E. winds are included. The displacement at rooftop and 11th floor of Mjøstårnet are extracted and post-processed to calculate total damping ratio ξ . For second scenario with ECG u_h profile, case 2a is applied with $T_g=5\text{s}$, $\Delta t_g=0\text{s}$, $u_{h,0}=11.1\text{m}\cdot\text{s}^{-1}$ and $u_g=10.9\text{m}\cdot\text{s}^{-1}$ equivalent to peak gust $22\text{m}\cdot\text{s}^{-1}$, while case 2b is based on $T_g=8\text{s}$, $\Delta t_g=3\text{s}$ with same $u_{h,0}$ and u_g . The displacements of building are extracted to investigate the aerodynamic response of building under gust. To investigate aerodynamic behaviour of Mjøstårnet under ambient environment after subjected to a gust, there are two challenges. First, when the BCs are initialized with a higher u_h (e.g. $11.1\text{m}\cdot\text{s}^{-1}$) and follow with a decreasing u_h , the flow solution will require significant number of time steps to converge after it reaches the ambient velocity (e.g. $2\text{m}\cdot\text{s}^{-1}$), and this post a major issue in coupling. Second, the FE model created in this study has difficulty to initialize at low surface pressure (correspond to low velocity e.g. $2\text{m}\cdot\text{s}^{-1}$) if non-linear analysis is chosen. This can be solved by initializing the BCs with ambient u_h (e.g. $2\text{m}\cdot\text{s}^{-1}$), followed by ramping up with an ECG profile, before coupled with the FEM with this adjusted ‘initial’ u_h value (case 3). The

displacements are extracted to investigate the aerodynamic response of building under gust followed by ambient environment.

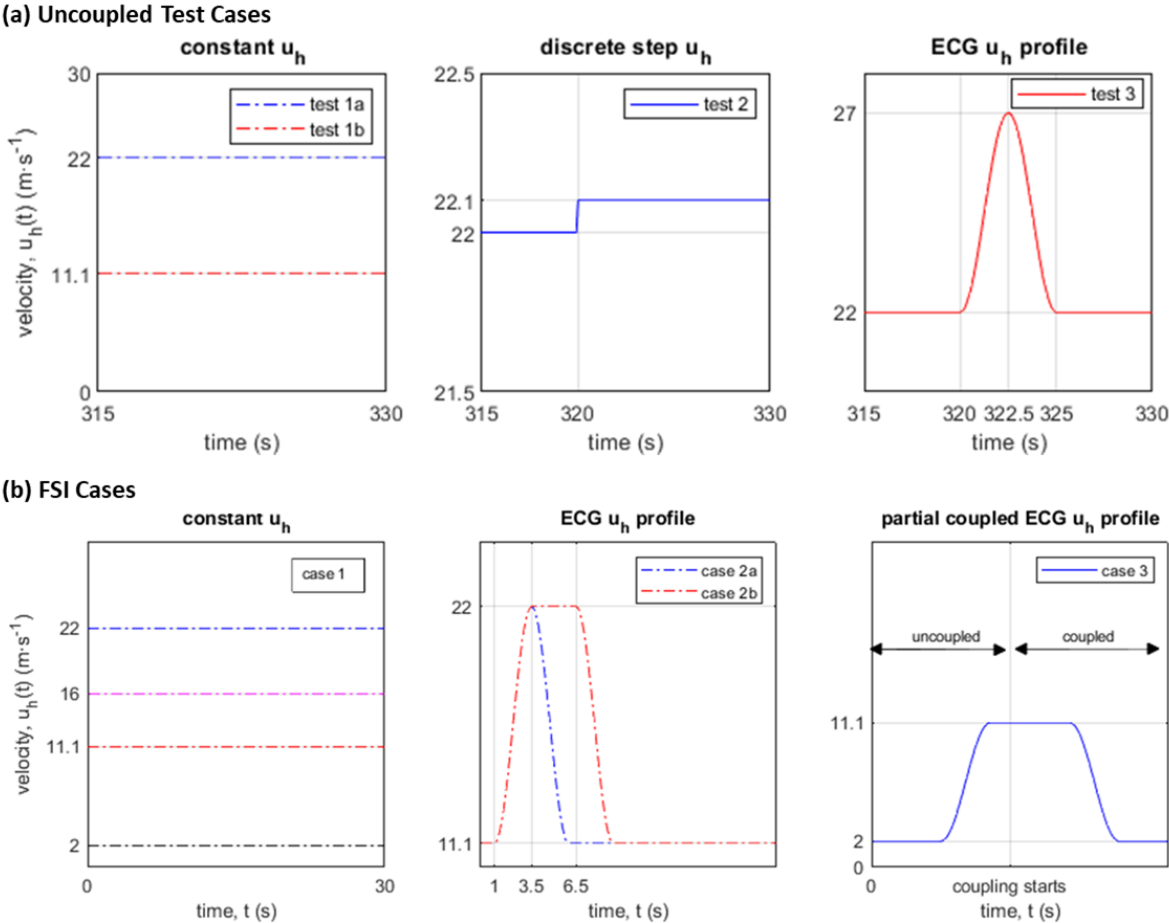


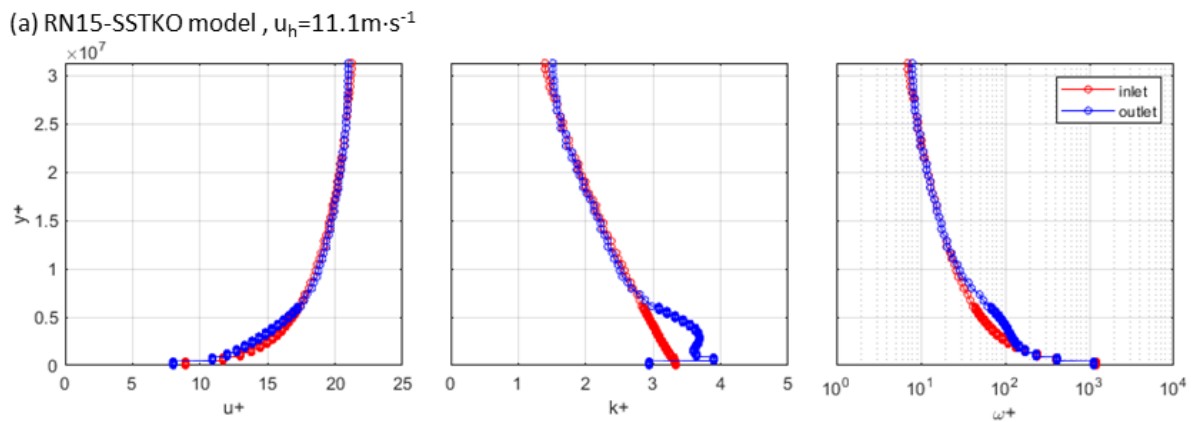
Figure 6 (a) uncoupled testing cases and (b) FSI cases

3. Results

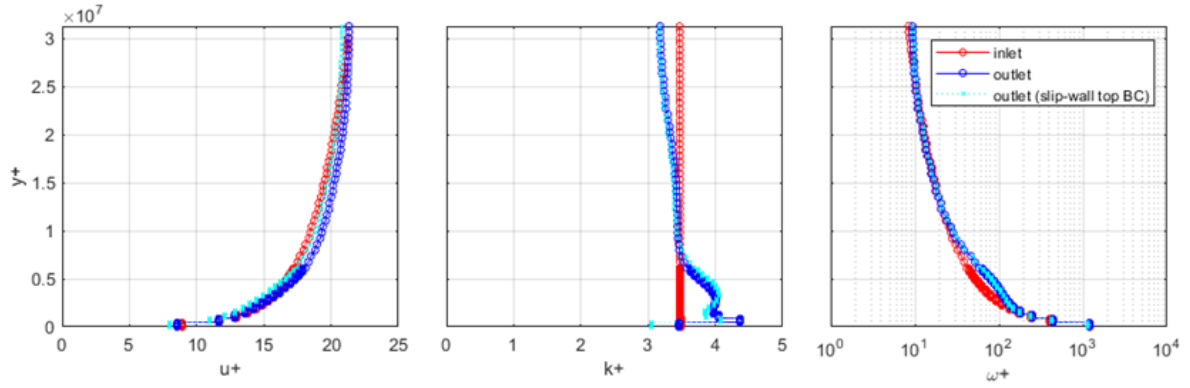
3.1. Selecting boundary conditions model

Under $u_h = 11.1 \text{ m}\cdot\text{s}^{-1}$ N.E. wind, both SSTKO models provide converged results by 2000 iterations, with RN15 achieves a rather conserved profiles between inlet and outlet compared to RN11 (Figure 7a and Figure 7b). Developed C_p profiles obtained from both SSTKO models, mapped in Figure 9a and plotted in Figure 8a. RN11-SSTKO with slip-wall top BC is included (Figure 7b) for comparison purpose. It is observed that by applying Eq.(19) to Eq.(21) at top BC under RN11-SSTKO, only slight improvements are obtained compared to using slip wall, which implies the top BC has failed to replicate the requirements of shear-driven models [31]. This might be due to incorrect setup of Neumann BC in the model. Simulation using SKE models have difficulty to converge, with solution diverges significantly from the beginning with high turbulence viscosity around the building. The convection scheme is reduced to first order for the first 1000 iterations to stabilize the flow solution, followed by second order convection scheme for the remaining 1000 iteration. This partial reduced scheme succeeds to suppress the divergence for RN15-SKE, however failed for RN11-SKE. Also, flow solution under RN15-SKE does not fully converge to an acceptable range at 2000 iteration.

Additional simulations are run with higher u_h with different direction, i.e. $u_h = 22 \text{ m}\cdot\text{s}^{-1}$ S.W., N.W. and S.E. winds using RN15-SSTKO model, while keeping the same domain size. Converged flow solutions are obtained, shown in Figure 9 and Figure 8b. No noteworthy irregularity is observed on the C_p profiles. In overall, RN15-SSTKO model generates an acceptable flow solution for the study of wind flow around a tall building with a rather detail features, e.g. balconies and top beam structures. It is decided that RN15-SSTKO is to be used as the BCs in this study.



(b) RN11-SSTKO model, $u_h=11.1\text{m}\cdot\text{s}^{-1}$



(c) RN15-SKE model, $u_h=11.1\text{m}\cdot\text{s}^{-1}$

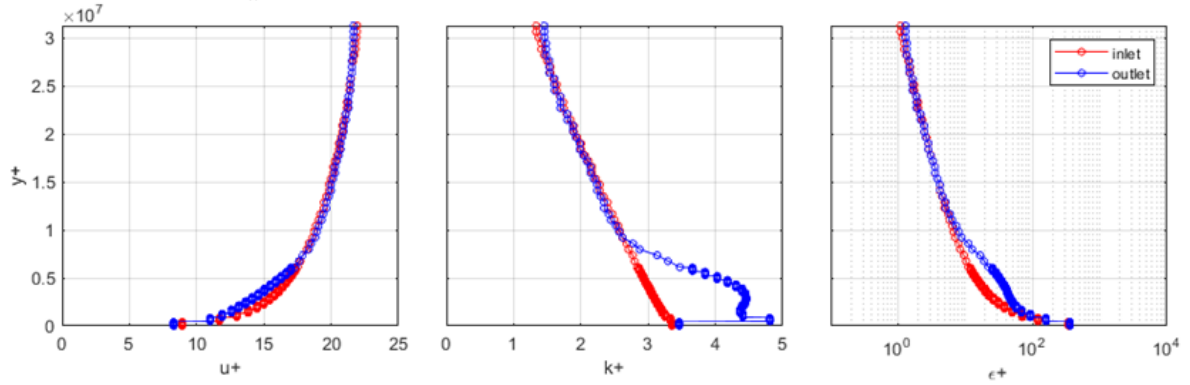
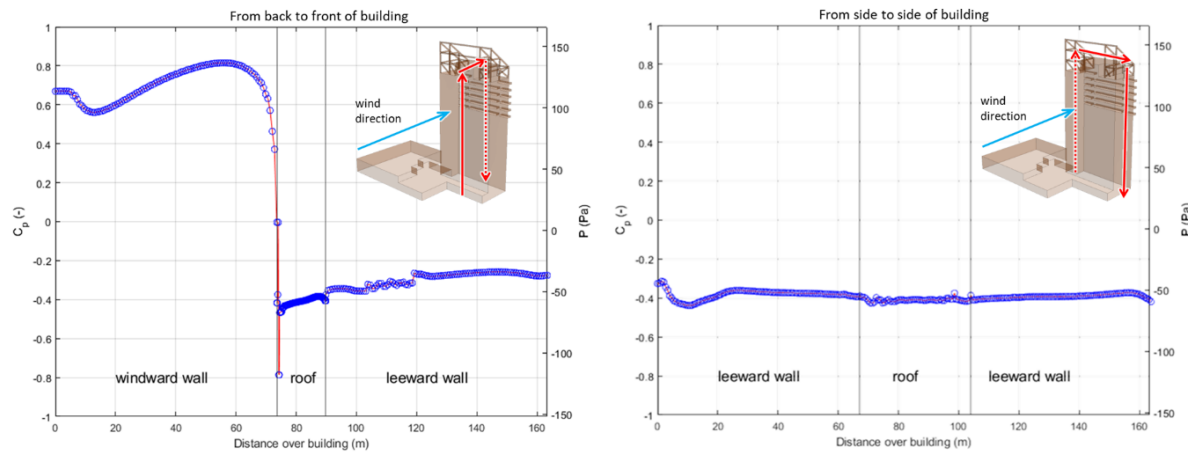


Figure 7 u^+ , k^+ , ϵ^+ and ω^+ profiles of inlet and outlet of CFD domain

(a) N.E. wind with back of building as windward, $u_h=11.1\text{m}\cdot\text{s}^{-1}$



(b) S.W. wind with front of building as windward, $u_h = 22\text{m}\cdot\text{s}^{-1}$

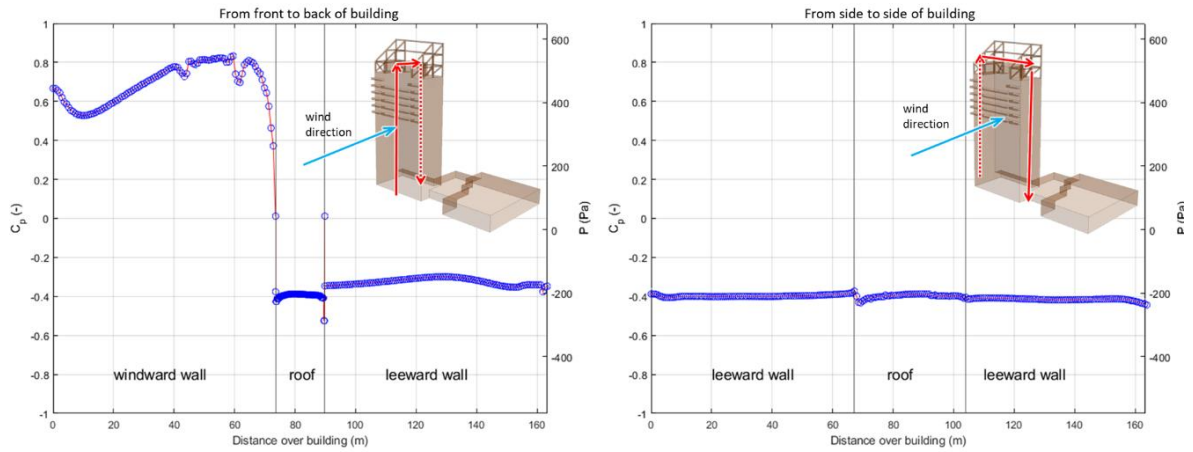


Figure 8 C_p and P profiles of Mjøstårnet

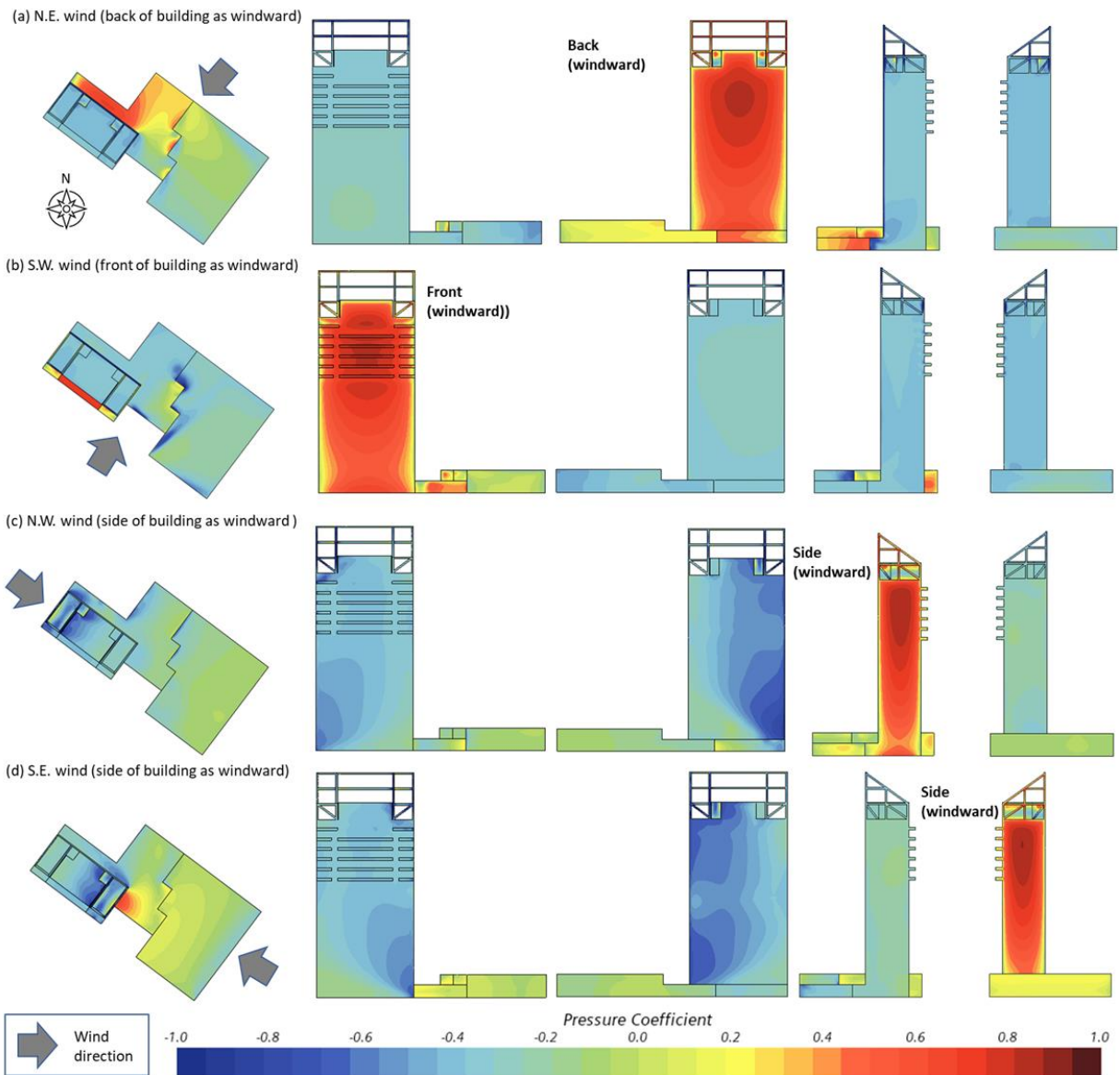
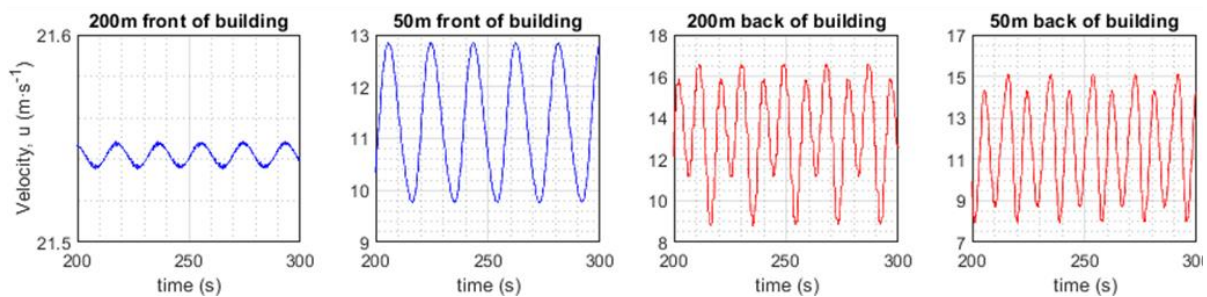


Figure 9 C_p profile of Mjøstårnet under SSTKO model

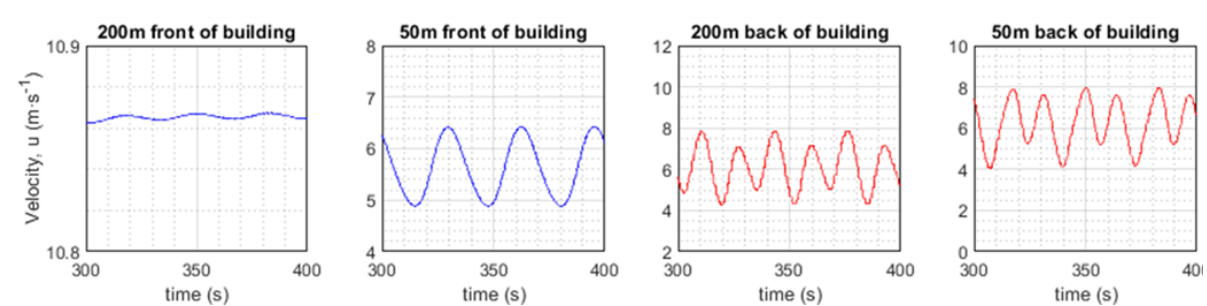
3.2. Uncoupled test cases

The transient U from test 1 at selected probes at 10m height are plotted in Figure 10a and Figure 10b. Under constant u_h profile, the wind flow is oscillating marginally at upstream, and amplified when approaching the building. Another observation is that the U profile is decaying from inlet to the building. Substantial fluctuations on the U profiles are observed at the downstream, mainly contributed by the vortex shedding around building. The frequency of upstream flow under $u_h=22\text{m}\cdot\text{s}^{-1}$ is around 0.5Hz, reduces to 0.2-0.3Hz under $u_h=11.1\text{m}\cdot\text{s}^{-1}$. Similarly, frequencies of downstream flow under $u_h=22\text{m}\cdot\text{s}^{-1}$ is higher than flow under $u_h=11.1\text{m}\cdot\text{s}^{-1}$. Oscillating pattern is also observed on the building surface pressure (Figure 10c).

a) Velocity profile at selected probe, $u_h=22\text{m}\cdot\text{s}^{-1}$



(b) Velocity profile at selected probe, $u_h=11.1\text{m}\cdot\text{s}^{-1}$



(c) Pressure profile (maximum magnitude) at windward and leeward walls

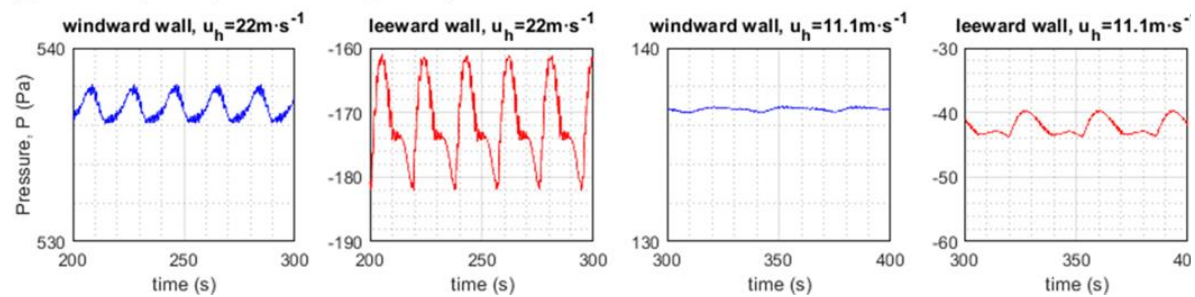


Figure 10 (a) and (b) Velocity profile of selected probes, (c) maximum surface pressure at windward and leeward walls

In test 2, a discrete change of u_h from $22.0\text{m}\cdot\text{s}^{-1}$ to $22.1\text{m}\cdot\text{s}^{-1}$ is tested with single time step $\Delta t=0.1\text{s}$ and 0.01s . The transient U at selected probes at 10m height are shown in Figure 11a. Both results under $\Delta t=0.1\text{s}$ and 0.01s are comparable and for that reason only $\Delta t=0.1\text{s}$ is presented. It is

apparent that the velocity field is updated instantaneously in the entire domain when there is a change of u_h . This instant update does not adhere to the conventional expectation that velocity correction will progress from upstream to downstream following the imposed wind speed, nonetheless it does not impede the study of structural behaviour under gust. The pressure field however failed to give a smooth transition when there is a shift on u_h (Figure 11b) under both $\Delta t=0.1s$ and $0.01s$. The pressure ‘jump’ with several order of magnitude and take 3 or more-time steps to converge back to the mean value. Similar situation is observed when tested with smaller time step $\Delta t=0.001s$, increased iterations within a time step, applied first order temporal discretization accuracy scheme or third order convection scheme, changed to RN11-SSTKO model or tested on a simple cubic model. The divergence of pressure field is plausibly due to large distance between inlet and building, combined with coarse meshing scheme. The requirement of using several time steps (where iterations within time step is not sufficient) to converge will post a hindrance in co-simulation, where erroneous pressure data will be feed from CFD to FEM during this converging process.

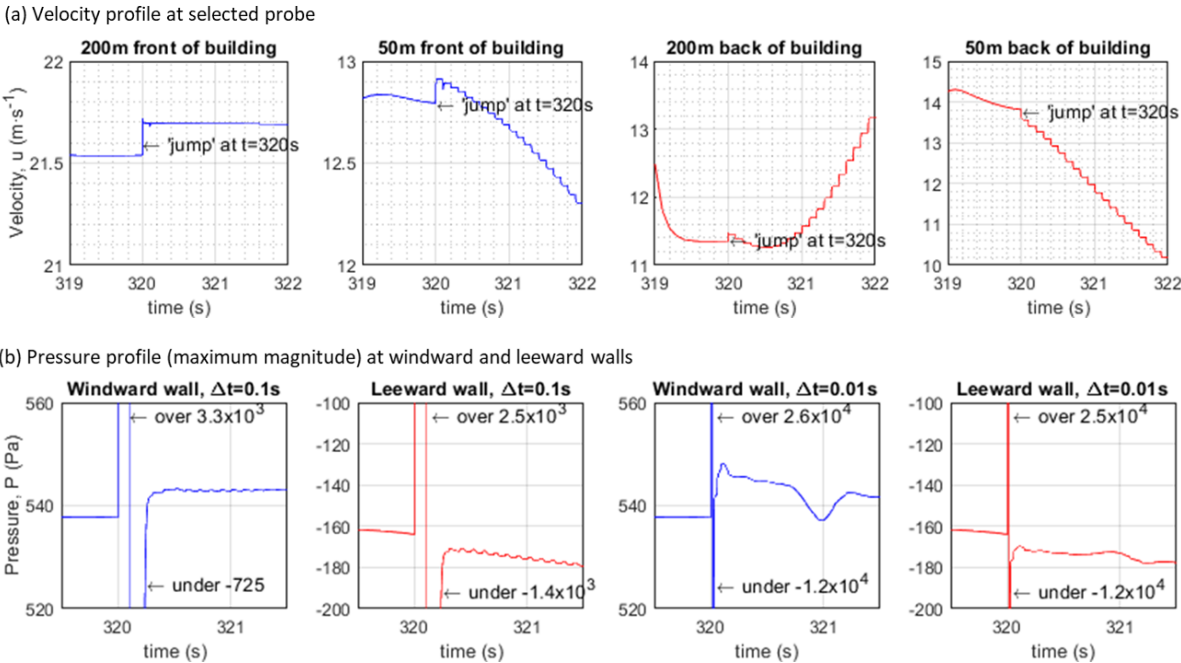
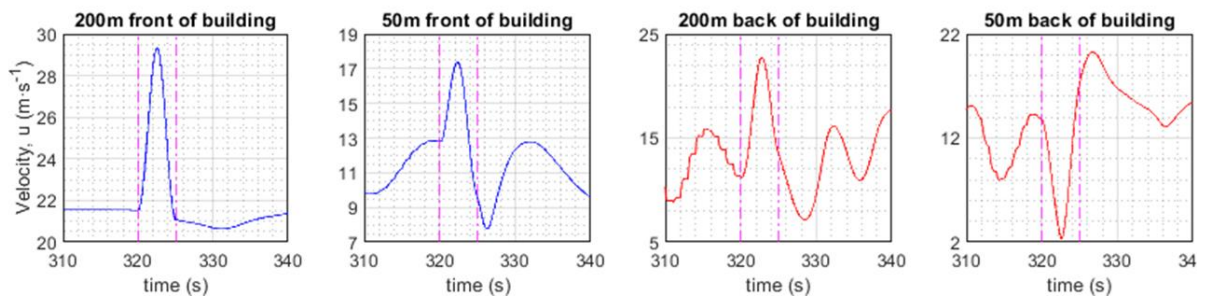


Figure 11 (a) Velocity profile at selected probes under $\Delta t=0.1s$, (b) maximum surface pressure at windward and leeward walls at $\Delta t=0.1s$ and $\Delta t=0.01s$

In test 3, time-varying ECG $u_h(t)$ profile is imposed, where $u_h(t)$ is updated every 0.1s with smaller simulation time step $\Delta t=0.01s$, i.e. $u_h(t)$ only adjusted for every 10-time steps. Similar to test 2, the transient U solution is updated instantaneously in the entire domain in response to change of u_h (Figure 12a), and the pressure fields are deviating up to four order of magnitude (Figure 12b left).

The pressure correction is loosely corresponding to the derivative of velocity profile, where a sine curve pressure trend is produced from the negative cosine $u_h(t)$ profile. The pressure data are further post-processed, i.e. only data at every tenth time step are accounted, and data from first to ninth time steps are treated as additional iterations for convergence purpose and omitted from analysis (Figure 12b). The post-processed surface pressures are responding proportionately to the change of velocity. This two-time steps' method is to be applied for subsequent FSI analysis, where smaller time steps are applied within CFD and FEM, conversely co-simulation is coupled and $u_h(t)$ is updated at larger time step, e.g. $\Delta t=0.01s$ used for numerical iterations, in conjunction with 0.1s for explicit coupling and u_h correction.

(a) Velocity profile at selected probe



(b) Maximum surface pressure profile of windward and leeward walls of the building

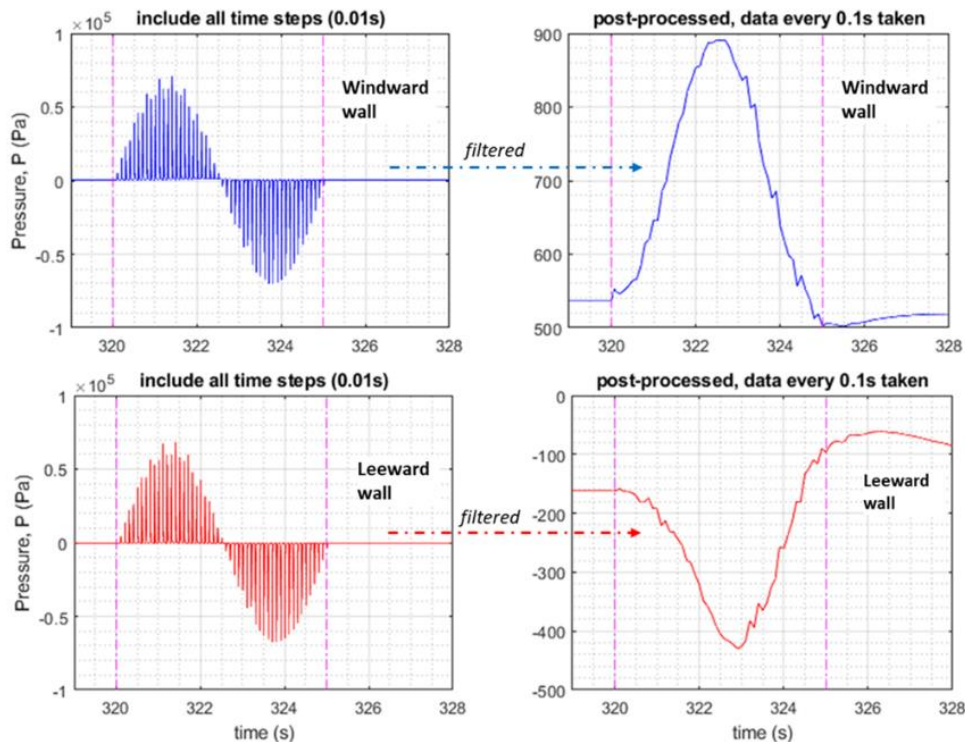


Figure 12 (a) Velocity profile at selected probes, (b) maximum surface pressure at windward and leeward walls, comparison is made between pre- and post-processed data.

3.3. FSI cases

Under Case 1 with a constant and continuous u_h profile, the relative displacement to mean d profiles at rooftop and 11th floor of Mjøstårnet are plotted in Figure 13. Total damping properties ξ of Mjøstårnet under different u_h and wind direction are calculated using relative displacements at selected peaks of vibration, and the median value are charted in Figure 14. Vibration under $u_h=2\text{m}\cdot\text{s}^{-1}$ is less than 0.1mm and thus omitted from analysis. The calculated ξ is up to 4.38%, however there is no noticeable pattern on the derived ξ when compared in term of different u_h , wind direction and probe location based on available simulated data.

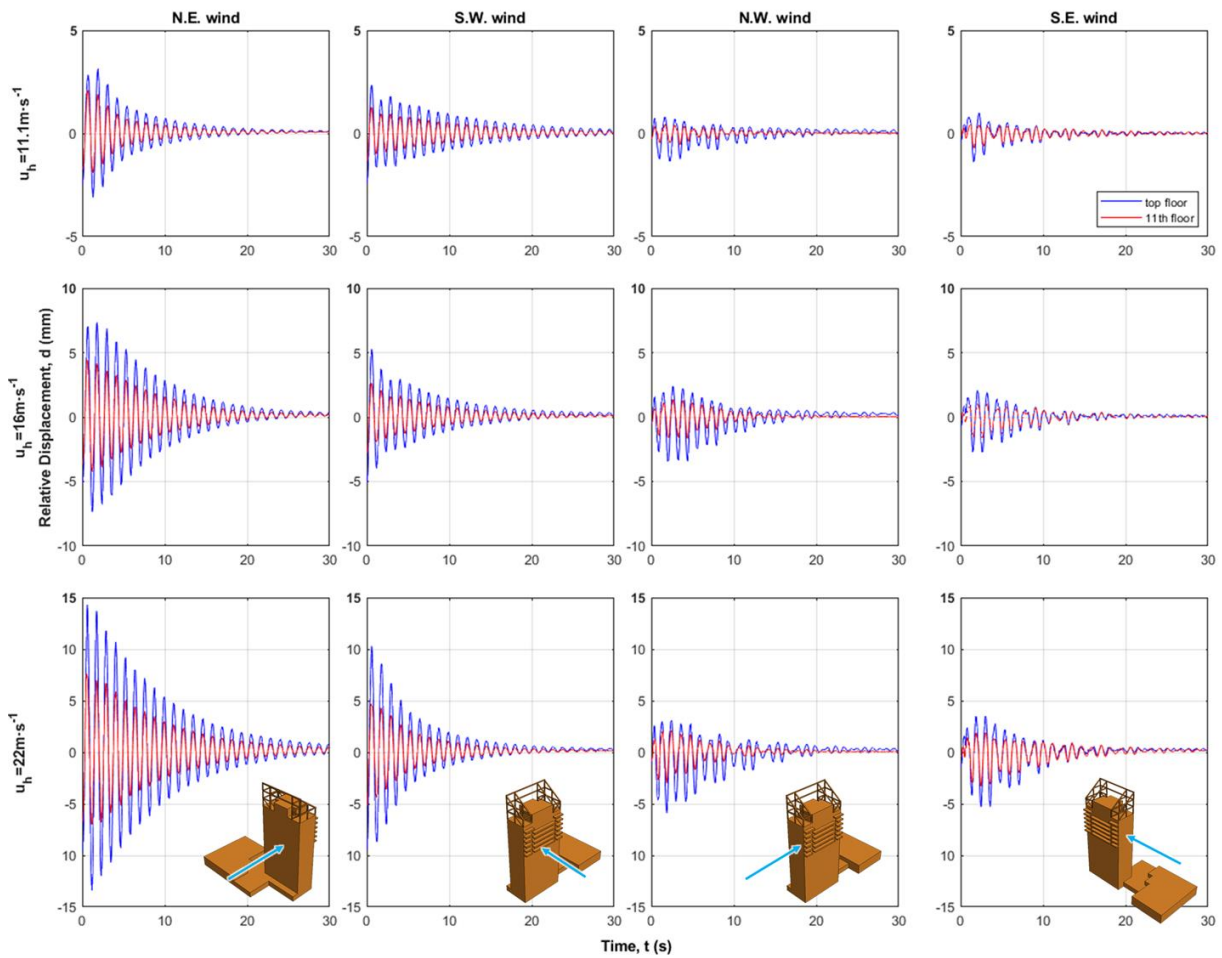


Figure 13 Relative displacements at rooftop and 11th floor of the building under case 1

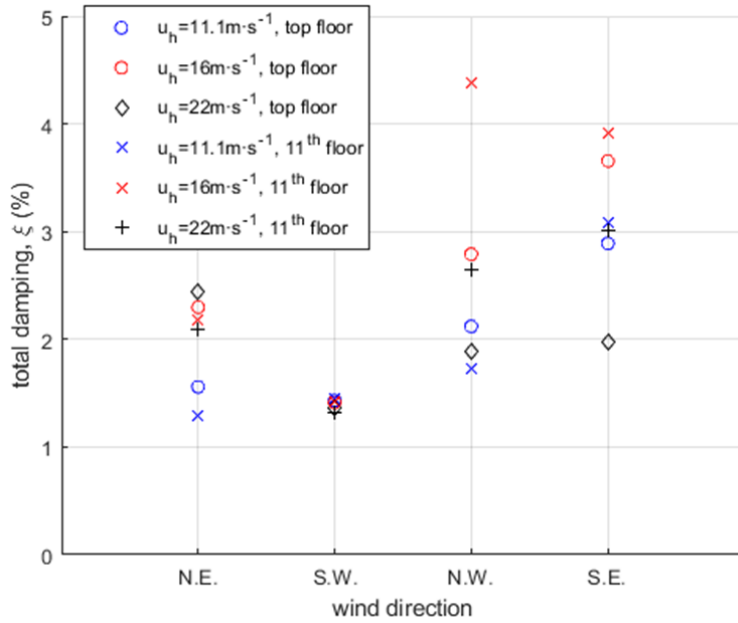
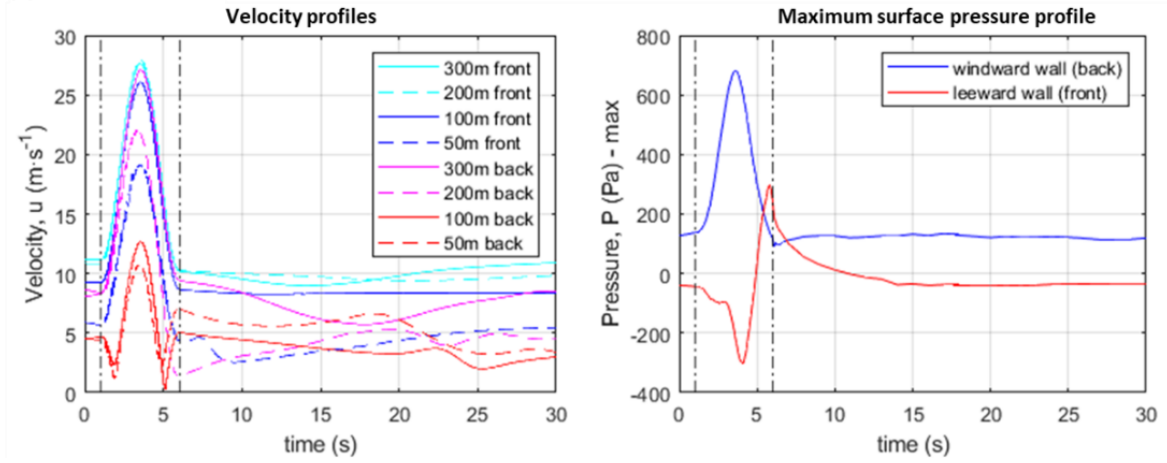


Figure 14 Total damping properties ξ of Mjøstårnet under different u_h and wind direction

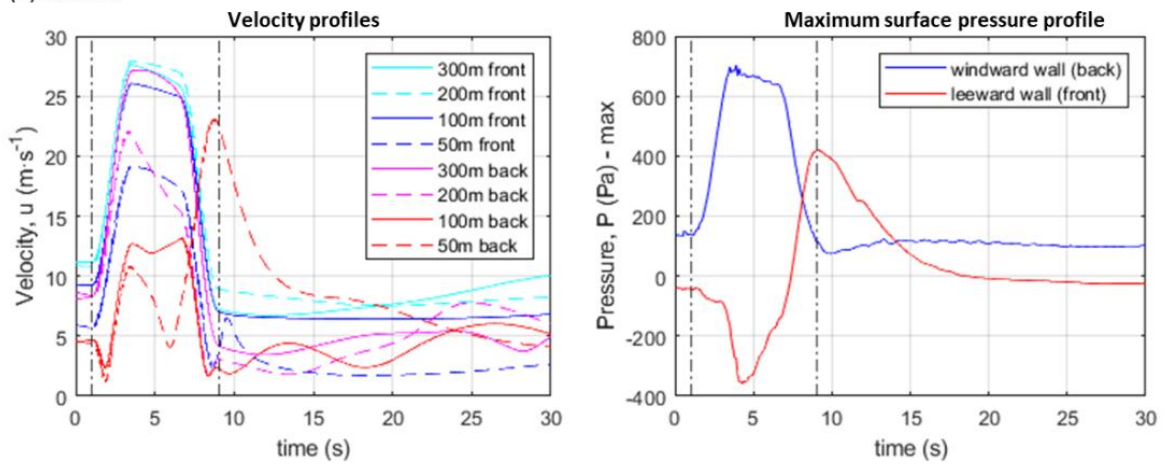
For Case 2 and 3 with time-varying $u_h(t)$ profiles, both transient U at selected probes and maximum building surface pressure at windward and leeward walls are plotted in Figure 15, and displacement at rooftop and 11th floor of Mjøstårnet are plotted in Figure 16. Similar to Test 3, flows in the whole domain react instantaneously following the shift in $u_h(t)$ profile. Steady couplings are achieved using the proposed two-time steps method, where smaller time steps are used for converging the solution prior coupled for data exchange between CFD and FEM.

Two distinct vibrations are produced with different peak gust duration Δt_g , i.e. 0s in Case 2a and 3s in Case 2b. Both cases react likewise during the gust period, however Case 2a produces a second resonance wave a few seconds after the end of gust and last around 20s (Figure 16a). The building vibrates at higher amplitude at lower frequency range when subjected to longer peak gust duration, while at lower gust duration the amplitude of vibration is comparable lower but is spread across a wider range of frequency. Under Case 3 with partial coupled $u_h(t)$ profile, the pressure fields are converging however not as smoothly once coupled. The surface pressure at the leeward wall takes roughly 20s to go below zero once the gust is removed. Building vibrations take longer time to be damped under ambient environment after a gust is imposed.

(a) Case 2a



(b) Case 2b



(c) Case 3

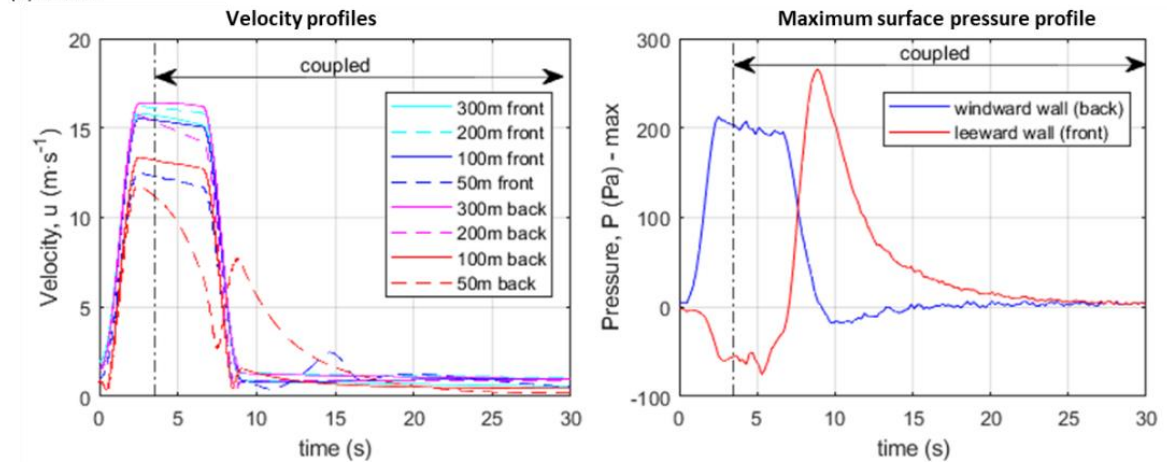


Figure 15 Velocity at selected probes and maximum surface pressure under (a) case 2a, (b) case2b, and (c) case 3

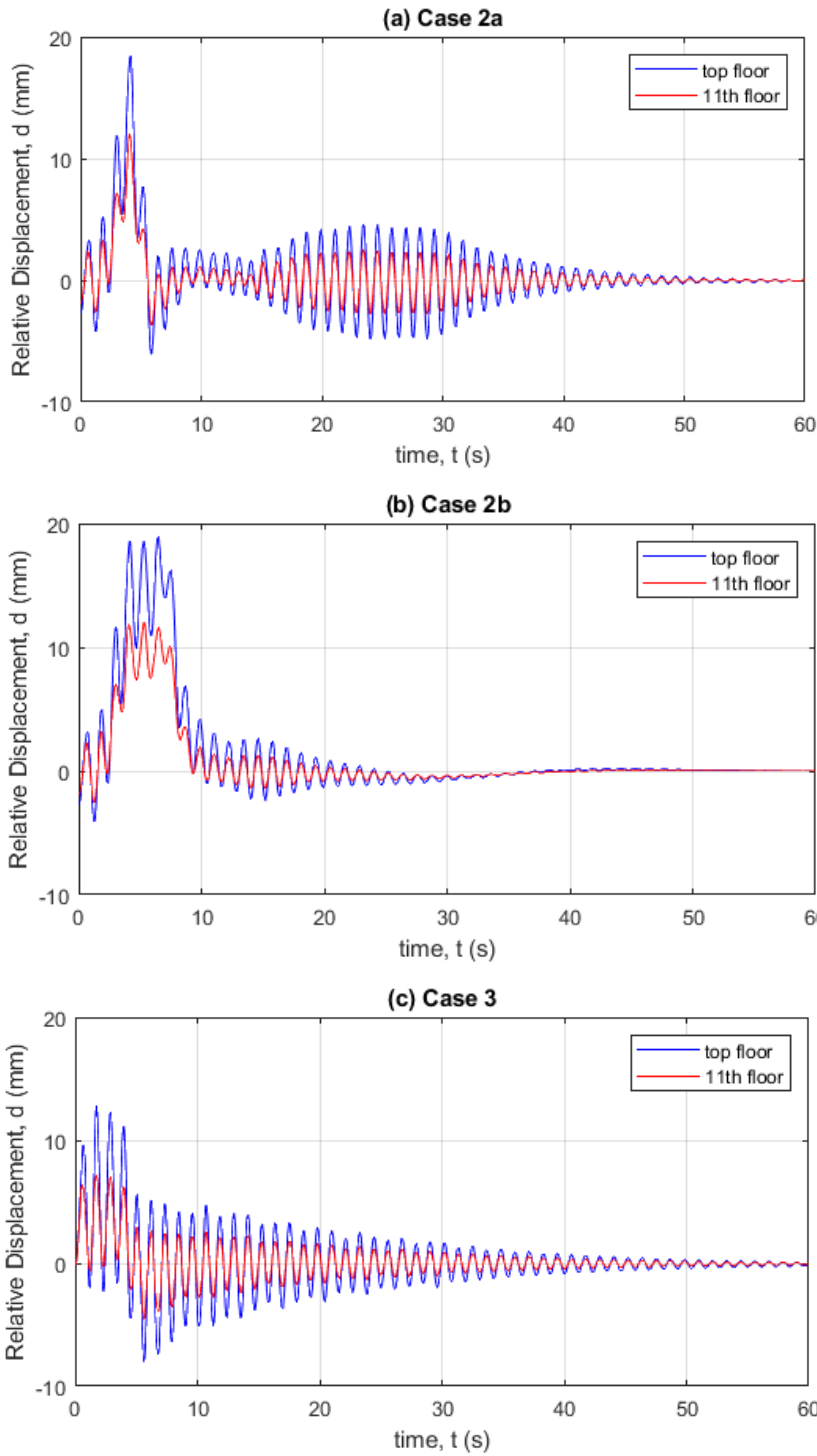


Figure 16 Relative displacement at rooftop and 11th floor of Mjøstårnet under (a) Case 2a, (b) Case 2b and (c) Case 3

4. Discussion

When employing unsteady RANS equations with SSTKO turbulence model, a constant u_h BC produces small but unsteady fluctuation at upstream flow. Larger fluctuations are formed for flow around the building caused by vortex shedding, this subsequently produces a time varying traction forces on building surface, allowing transient or quasi transient analysis of wind action on building. Another attribute of transient U profile is the decaying of its mean U from inlet to the building model, it is therefore necessary to adjust the u_h profile if specific wind speed around building is desired.

The ABL is modelled as incompressible by use of constant density gas model. However incompressible model allows the flow field to update and propagate instantaneously in the whole domain when change is made at BCs. This numerical behaviour can be disregarded if a time-independent inflow profile is given, i.e. constant u_h , however this posts a major issue if time-varying inflow profile such as gust is imposed. RGA method is utilized in this study, however several challenges are confronted, i.e. large distance between inlet and building, substantial domain size, and a comparable rough mesh. The pressure field failed to give a smooth progression when there is a change at inflow profile, with several orders of magnitude deviation and takes a number of time steps to converge back to mean value. A two-time steps strategy is made to resolve this deviation, e.g. smaller time steps within CFD and FEM, but $u_h(t)$ profile is updated at larger time step, and the explicit coupling is set similar to the bigger time step used for $u_h(t)$ correction. The time steps in between the coupling are treated as additional iteration for convergence purpose. While this is not an elegant solution, this method successfully resolves the problem, where pressure field is responding proportionally to the change of velocity.

Another approach not tested in this study is to use source term formulation to inject wind gusts into the flow domain. One cost-effective solution has been proposed by Nayer and Breuer (2020) [54], where the source-term is derived for momentum conservation equation and nothing is added to the continuity equation, thus ensuring both local and global mass conservation and avoid divergence from the simulation. Their injected gust travels through the flow field with nearly constant propagation velocity, and the generated flow field is deemed satisfactory. The proposed formulation is tested using LES however it is suggested that it can be combined with URANS solver. This method is proposed to be included in future study.

In order to simulate aerodynamic response of a building accurately, it is necessary to model the building on individual elementary level instead of a simple solid elastic bluff body. One critical aspect of the building which is not fully modelled is the soil-structure interaction. This shortfall reflects on the lower damping ratio compared to the 1.9% designed damping ratio. The building

model is also comparable 'stiff' when referring to the design value. The FE model is however considered acceptable for the purpose of demonstrating two-way coupled FSI co-simulation application here.

Surface-to-surface mapping is used to couple the building model in both FEM and CFD. It is a rather straightforward exercise, by exporting the CAD model from FEM into CFD, thus ensuring a seamless mapping during co-simulation. However this method requires modelling of building envelope and other non-structural elements in the FE model, and consequently complicated the dynamic analysis within the FEM, especially the tie-in between structural and non-structural members. It is therefore suggested a beam-to-surface mapping strategy should be used in subsequent study to avoid modelling of non-structural members in FEM, i.e. nodal displacement and rotation of the beam elements from the FE model are mapped onto the vertices of corresponded surface in CFD.

5. Summary and conclusion

The main objective of this study is to explore an inexpensive method to perform aerodynamic analysis of tall building using two-way coupled CFD-FEM co-simulation. This is realized by drawing on URANS equations with SSTKO turbulence model to simulate the wind flow, combined with the pressure-driven boundary conditions proposed by Richard and Norris (2015) [32].

The FSI analysis is tested on Mjøstårnet under two different wind profiles, one with constant u_h profile and another with a time-varying $u_h(t)$ profile like gust. This study has demonstrated possibility to calculate the total damping of building including aerodynamic, e.g. the simulated ξ of Mjøstårnet is up to 4.38% under different wind conditions and probe locations. For time-varying $u_h(t)$ profile such as gust, it is proposed to use smaller time steps within both CFD and FEM, but bigger time step is used to update the inflow $u_h(t)$ profile and explicit coupling in co-simulation. The time steps in between the update/coupling are treated as additional iteration for convergence purpose. This approach successfully enables the use of URANS with a rather rough mesh in a more complex and realistic aerodynamic analysis. The number of cells used in this study is economic with less than 3 million in CFD, and one FSI simulation takes only approximately 200-400 core hours. This allows a repeatable FSI analysis with different building models and boundary conditions.

References

- [1] E. Simiu and D. Yeo, "Computational Wind Engineering," in *Wind Effects on Structures: Modern Structural Design for Wind 4th edition*, Wiley Blackwell, 2019, p. 135.
- [2] H. Versteeg and W. Malalasekera, "Turbulence and its modelling," in *An Introduction to Computational Fluid Dynamics - The Finite Volume Method*, Harlow, Pearson Education, 2007, pp. 40-113.
- [3] B. Blocken, "Computational Fluid Dynamics for urban physics: Importance, scales, possibilities, limitations and ten tips and tricks towards accurate and reliable simulations," *Building and Environment*, vol. 91, pp. 219-245. doi:10.1016/j.buildenv.2015.02.015, 2015.
- [4] Y. Tominaga, "Flow around a high-rise building using steady and unsteady RANS CFD: Effect of large-scale fluctuations on the velocity statistics," *Journal of Wind Engineering & Industrial Aerodynamics*, vol. 142, p. 93–103. doi:10.1016/j.jweia.2015.03.013, 2015.
- [5] R. Heinrich and L. Reimer, "Comparison of different approaches for gust modelling in the CFD Code Tau," DLR Institute of Aerodynamics and Flow Technology, Braunschweig, 2013.
- [6] A. Langer-Moller, "Simulation of transient gusts on the NREL 5MW wind turbine using the URANS solver THETA," *European Academy of Wind Energy e.V.*, vol. 3, pp. 461–474. doi:10.5194/wes-3-461-2018, 2018.
- [7] L. Menegozzo, A. D. Monte, E. Benini and A. Benato, "Small wind turbines: A numerical study for aerodynamic performance assessment under gust conditions," *Renewable Energy*, vol. 121, pp. 123-132. doi:10.1016/j.renene.2017.12.086, 2018.
- [8] A. L. Braun and A. M. Awruch, "Aerodynamic and aeroelastic analyses on the CAARC standard tall building model using numerical simulation," *Computers and Structures*, vol. 87, p. 564–581. doi:10.1016/j.compstruc.2009.02.002, 2009.
- [9] Y. Zhang, W. G. Habashi and R. A. Khurram, "Predicting wind-induced vibrations of high-rise buildings using unsteady CFD and modal analysis," *Journal of Wind Engineering and Industrial Aerodynamics*, vol. 136, p. 165–179. doi:10.1016/j.jweia.2014.11.008, 2015.
- [10] K. Wijesooriya, D. Mohotti, A. Amin and K. Chauhan, "An uncoupled fluid structure interaction method in the assessment of structural responses of tall buildings," *Structures*, vol. 25, p. 448–462. doi:10.1016/j.istruc.2020.03.031, 2020.

- [11] J. Seo, W. Schaffer, M. Head and M. S. & E. Choi, "Integrated FEM and CFD Simulation for Offshore Wind Turbine Structural Response," *International Journal of Steel Structures*, vol. 19, no. 4, pp. 1112–1124. doi:10.1007/s13296-018-0191-y, 2019.
- [12] K. Lee, Z. Huque, R. Kommalapati and S.-E. Han, "Fluid-structure interaction analysis of NREL phase VI wind turbine: Aerodynamic force evaluation and structural analysis using FSI analysis," *Renewable Energy*, vol. 113, pp. 512-531. doi:10.1016/j.renene.2017.02.071, 2017.
- [13] D. Oliveira, A. Santiago and C. Rigueiro, "Fluid structure interaction in offshore environment," *INEGI/FEUP. Proceedings of the 5th International Conference on Integrity-Reliability-Failure*, pp. 635-646, 2016.
- [14] H. Zhang, L. Liu, M. Dong and H. Sun, "Analysis of wind-induced vibration of fluid–structure interaction system for isolated aqueduct bridge," *Engineering Structures*, vol. 46, p. 28–37. doi:10.1016/j.engstruct.2012.07.019, 2013.
- [15] A. Braun and A. Awruch, "Finite element simulation of the wind action over bridge sectional models: Application to the Guamá River Bridge (Pará State, Brazil)," *Finite Elements in Analysis and Design*, vol. 44, p. 105–122. doi:10.1016/j.finel.2007.11.006, 2008.
- [16] J. Alos-Moya, I. Paya-Zaforteza, M. Garlock, E. Loma-Ossorio, D. Schiffner and A. Hospitaler, "Analysis of a bridge failure due to fire using computational fluid dynamics and finite element models," *Engineering Structures*, vol. 68, p. 96–110. doi:10.1016/j.engstruct.2014.02.022, 2014.
- [17] J. C. Silva and A. Landesmann, "Performance-based analysis of steel–concrete composite floor exposed to fire," *Journal of Constructional Steel Research*, vol. 83, p. 117–126. doi:10.1016/j.jcsr.2013.01.009, 2013.
- [18] J. d. Boer, H. Hofmeyer, J. Maljaars and R. v. Herpen, "Two-way coupled CFD fire and thermomechanical FE analyses of a self-supporting sandwich panel façade system," *Fire Safety Journal*, vol. 105, p. 154–168. doi:10.1016/j.firesaf.2019.02.011, 2019.
- [19] J. Feenstra, H. Hofmeyer, R. V. Herpen and M. Mahendran, "Automated two-way coupling of CFD fire simulations to thermomechanical FE analyses at the overall structural level," *Fire Safety Journal*, vol. 96, p. 165–175. doi:10.1016/j.firesaf.2017.11.007, 2018.
- [20] "Norsk KlimaServiceSenter," Meteorologisk institutt, [Online]. Available: <https://seklima.met.no/observations/>. [Accessed 23 2021].
- [21] Siemens Industry Software Inc., *User manual for Simcenter™ STAR-CCM+™ software*, 2020.2 (15.04.008-R8), 2020.
- [22] Dassault Systemes, "Abaqus Analysis User's Guide Volume I, II, III, IV and V," 2016.

- [23] W. P. Jones and B. E. Launder, "The Prediction of Laminarization with a Two Equation Model of Turbulence," *International journal of heat and mass transfer*, vol. 15, no. 2, pp. 301-314, 1972.
- [24] B. E. Launder and D. B. Spalding, "The numerical computation of turbulent flows," *Computer Methods in Applied Mechanics and Engineering*, vol. 3, pp. 269-289, 1974.
- [25] F. R. Menter, "Two-Equation Eddy-Viscosity Turbulence Models for Engineering Applications," *AIAA Journal*, vol. 32, no. 8, pp. 1598-1605. doi:10.2514/3.12149, 1994.
- [26] R. Cook, D. Malkus, M. Plesha and R. Witt, "Finite Elements in Structural Dynamics and Vibrations," in *Concepts and Applications of Finite Element Analysis, 4th edition*, Madison, John Wiley & Sons, Inc, 2002, pp. 373-443.
- [27] CEN, "NS-EN 14080:2013 Timber structures - Glued laminated timber and glued solid timber - Requirements," 2016.
- [28] R. Abrahamsen, "Mjøstårnet – Construction of an 81 m tall timber building," *Internationales Holzbau-Forum IHF 2017*, p. 23, 2017.
- [29] P. Richards and R. Hoxey, "Appropriate boundary conditions for computational wind engineering models using the k- ϵ turbulence model," *Journal of Wind Engineering and Industrial Aerodynamics*, Vols. 46-47, pp. 145-153. doi:10.1016/0167-6105(93)90124-7, 1993.
- [30] A. Davenport, C. S. B. Grimmond, T. Oke and J. Wieringa, "Estimating The Roughness of Cities and Sheltered Country. 12th Applied Climatology.," *American Meteorological Society*, pp. 96-99, 2000.
- [31] P. Richards and S.E.Norris, "Appropriate boundary conditions for computational wind engineering models revisited," *Journal of Wind Engineering and Industrial Aerodynamics*, no. 99, pp. 257-266. doi:10.1016/j.jweia.2010.12.008, 2011.
- [32] P. Richards and S.E.Norris, "Appropriate boundary conditions for a pressure driven boundary layer," *Journal of Wind Engineering and Industrial Aerodynamics*, vol. 142, pp. 43-52. doi:10.1016/j.jweia.2015.03.003, 2015.
- [33] International Electrotechnical Commission IEC, *IEC 61400-1 Wind energy generation systems - Part 1: Design requirements*, 2019.
- [34] B. Blocken, T. Stathopoulos and J. Carmeliet, "CFD simulation of the atmospheric boundary layer: wall function problems," *Atmospheric Environment*, vol. 41, no. 2, pp. 238-252. doi:10.1016/j.atmosenv.2006.08.019, 2007.
- [35] B. Blocken, T. Stathopoulos and J. Carmeliet, "CFD evaluation of wind speed conditions in passages between parallel buildings—effect of wall-function roughness modifications for the

- atmospheric boundary layer flow," *Journal of Wind Engineering and Industrial Aerodynamics*, vol. 95, no. 9-11, pp. 941-962. doi:10.1016/j.jweia.2007.01.013, 2007.
- [36] D. Hargreaves and N. Wright, "On the use of the k-e model in commercial CFD software to model the neutral atmospheric boundary layer," *Journal of Wind Engineering and Industrial Aerodynamics*, vol. 5, no. 95, pp. 355-369. doi:10.1016/j.jweia.2006.08.002, 2007.
- [37] J. O'Sullivan, R. Archer and R. Flay, "Consistent boundary conditions for flows within the atmospheric boundary layer," *Journal of Wind Engineering and Industrial Aerodynamics*, no. 99, p. 65-77. doi:10.1016/j.jweia.2010.10.009, 2011.
- [38] X. Zhang, "CFD simulation of neutral ABL flows," *Danmarks Tekniske Universite, Risø Nationallaboratoriet for Bæredygtig Energi*, 2009.
- [39] CEN, "Eurocode 0: Basis of structural design EN 1990:2002+A1," Brussels, 2005.
- [40] CEN, "Eurocode 1: Actions on structures - Part 1-1: General actions - Densities, self-weight, imposed loads for buildings EN1991-1-1," Brussels, 2002.
- [41] T. Reynolds, R. Harris and W.-S. Chang, "Viscoelastic embedment behaviour of dowels and screws in timber under in-service vibration," *European Journal of Wood and Wood Products*, vol. 71, pp. 623-634. doi:10.1007/s00107-013-0720-5, 2013.
- [42] CEN, "Eurocode 5: Design of timber structures - Part 1-1: General - Common rules and rules for buildings EN 1995-1-1 :2004," CEN, Brussels, 2004.
- [43] J. Porteous and A. Kermani, "Moment Capacity of Connections Formed with Metal Dowel Fasteners or Connectors," in *Structural Timber Design to Eurocode 5. 2nd edition*, Wiley-Blackwell, 2013, pp. 504-526.
- [44] I. Edskär and H. Lidelöw, "Dynamic properties of cross-laminated timber and timber truss building systems," *Engineering Structures*, vol. 186, pp. 525-535. doi:10.1016/j.engstruct.2019.01.136, 2019.
- [45] A. Feldmann, H. Huang, W. Chang, R. Harris, P. Dietsch, M. Gräfe and C. Hein, "Dynamic properties of tall timber structures under wind-induced vibration," in *World Conference on Timber Engineering*, Vienna, 2016.
- [46] N. Labonnote, A. Rønquist and K. A. Malo, "Modified hysteretic damping model applied to Timoshenko timber beams.," *Computers & Structures*, vol. 121, pp. 22-31. doi:10.1016/j.compstruc.2013.03.008, 2013.

- [47] N. Labonnote, A. Rønquist and K. A. Malo, "Experimental evaluations of material damping in timber beams of structural dimensions," *Wood Science and Technology*, vol. 47, p. 1033–1050, 2013.
- [48] CEN, "ISO 10137 Bases for design of structures - Serviceability of buildings and walkways against vibrations," 2007.
- [49] P. Landel, A. Linderholt and M. Johansson, "Dynamical properties of a large glulam truss for a tall timber building," in *2018 World Conference on Timber Engineering*, Seoul, 2018.
- [50] T. Reynolds, R. Harris and W.-S. Chang, "Dynamic stiffness and damping of dowel-type connections for timber structures under service conditions," in *2012 World Conference on Timber Engineering*, Auckland, 2012.
- [51] K. A. Malo, R. B. Abrahamsen and M. A. Bjertnæs, "Some structural design issues of the 14-storey timber framed building "Treet" in Norway," *European Journal of Wood and Wood Products*, vol. 74, pp. 407–424. doi:10.1007/s00107-016-1022-5, 2016.
- [52] H. M. Hilber, T. J. R. Hughes and R. L. Taylor, "Improved Numerical Dissipation for Time Integration Algorithms in Structural Dynamics," *Earthquake Engineering and Structural Dynamics*, vol. 5, p. 283–292. Permalink:escholarship.org/uc/item/18z548gt, 1976.
- [53] CEN, "Eurocode 1: Actions on structures Part 1-4: General actions - Wind actions (NS EN 1991-1-4:2005)," CEN, Brussels, 2009.
- [54] G. Nayer and M. Breuer, "A source-term formulation for injecting wind gusts in CFD simulations," *Journal of Wind Engineering and Industrial Aerodynamics*, vol. 207, p. 104405. doi:10.1016/j.jweia.2020.104405, 2020.
- [55] P. Richards, R. Hoxey and L.J. Short, "Wind pressures on a 6m cube," *Journal of Wind Engineering and Industrial Aerodynamics*, Vols. 14-15, no. 89, pp. 1553-1564. doi:10.1016/S0167-6105(01)00139-8, 2001.
- [56] H. C. Lim, T. G. Thomas and I. P. Castro, "Flow around a cube in a turbulent boundary layer LES and experiment," *Journal of Wind Engineering and Industrial Aerodynamics*, vol. 97, p. 96–109. doi:10.1016/j.jweia.2009.01.001, 2009.

Appendices

A. Effective terrain roughness y_0

Table 3 Davenport classification of effective terrain roughness

Cat	y_0	Landscape description
1	0.0002	'Sea'. Open sea or lake, tidal flat, snow-covered flat plain, featureless desert, tarmac and concrete with a free fetch of several kilometres.
2	0.005	'Smooth'. Featureless land surface without any noticeable obstacles and with negligible vegetation, e.g. beaches, pack ice without large ridges, marsh, snow-covered or fallow open country.
3	0.03	'Open'. Level country with low vegetation (e.g. grass) and isolated obstacles with separations of at least 50 obstacle heights, e.g. grazing land without windbreaks, heather, moor and tundra, runway area of airports, ice with ridges crosswind.
4	0.10	'Roughly open'. Cultivated or natural area with low crops or plant covers, or moderately open country with occasional obstacles (e.g. low hedges, isolated low buildings or trees) at relative horizontal distances of at least 20 obstacle height.
5	0.25	'Rough'. Cultivated or natural area with high crops or crops of varying height, and scattered obstacles at relative distances of 12-15 obstacle heights for porous objects (e.g. shelterbelts) or 8-12 obstacle height for low solid objects (e.g. buildings)
6	0.5	'Very rough'. Intensively cultivated landscape with many rather large obstacle groups (large farms, slumps of forest) separated by open spaces of about 8 obstacle heights. Low densely planted major vegetation like bushland, orchards, young forest. Area moderately covered by low buildings with interspaces of 3-7 building heights and no high trees.
7	1.0	'Skimming'. Landscape regularly covered with similar-size large obstacles, with open spaces of the same order of magnitude as obstacle height, e.g. mature regular forests, densely built-up area without much building height variation.
8	≥ 2	'Chaotic'. City centres with mixture of low-rise and high-rise buildings, or large forests of irregular height with many clearings.

B. BIM model of Mjøstårnet

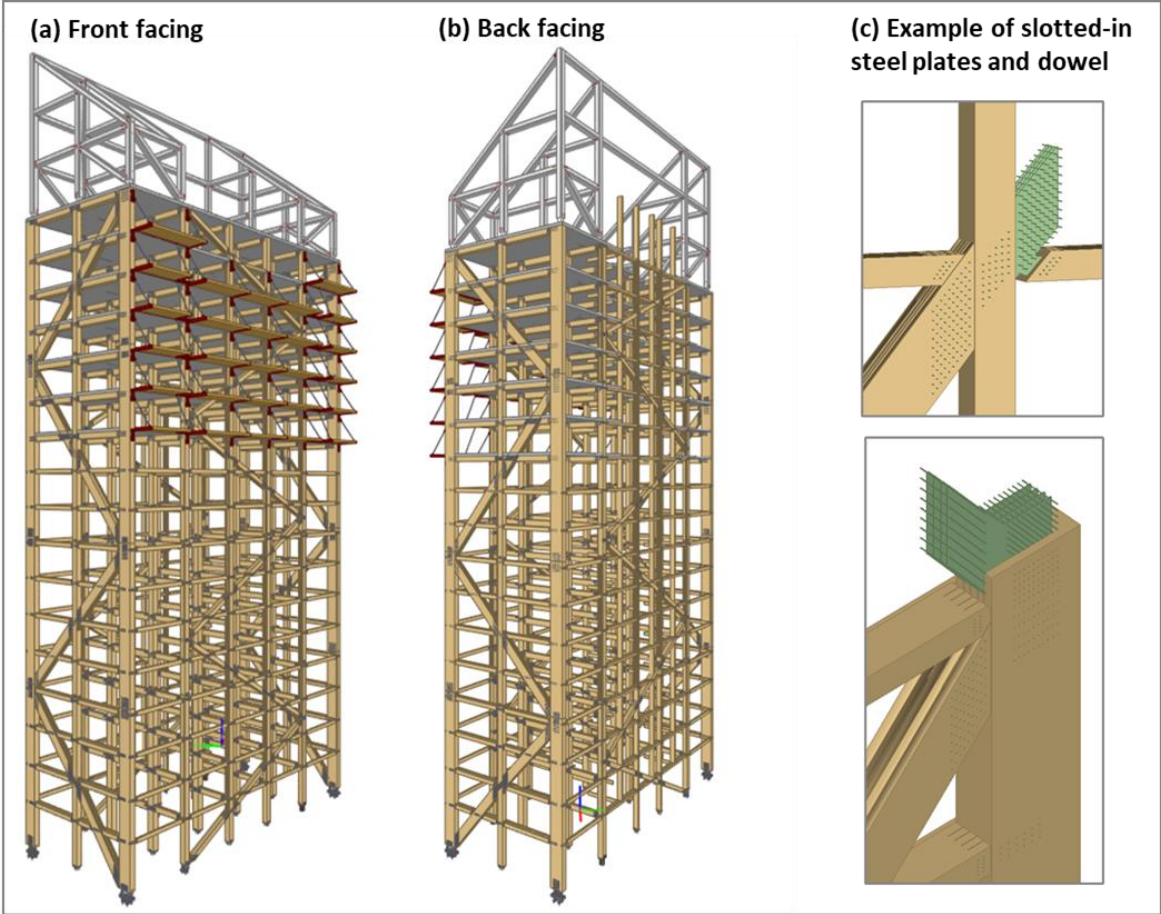


Figure 17 BIM of Mjøstårnet

C. Properties assigned in FE model

Table 4 Stiffness of connections of Mjøstårnet assigned in FEM

No.	n_{sp}	n_{dowel}	$K_{ser,d} (x10^6 N \cdot m^{-1})$	$K_{ser,\theta} (x10^6 N \cdot m \cdot rad^{-1})$	Type
1	8	8x5	2977	191	bracing to column #1
2	8	9x9	6029	1201	bracing to column #2
3	4	4x3	447	6	bracing to beam #1
4	8	2x5	744	11	bracing to beam #2
5	8	10x8	5955	942	column to column #1
6	8	5x1	372	4	column to column #2
7	4	4x3	447	3	beam to column #1
8	8	2x5	744	7	beam to column #2
9	4	2x6	447	7	beam to column #3
10	4	4x7	1042	42	beam to column #4
11	8	10x10	7444	1058	column to foundation #1

Table 5 Damping coefficient of connections of Mjøstårnet assigned in FEM

Sr. No.	$C_{22}=C_{33} (x10^6 N \cdot s \cdot m^{-1})$	$C_{44} (x10^6 N \cdot m \cdot s \cdot rad^{-1})$
1	36.136	2.317
2	73.175	14.577
3	5.420	0.067
4	9.034	0.132
5	72.271	11.426
6	4.517	0.044
7	5.420	0.035
8	9.034	0.081
9	5.420	0.084
10	12.647	0.515
11	90.339	12.838

To verify the effect of damping properties assigned to FE model using direct solution dynamic analysis procedure in Abaqus, different FE models are included, i.e. model without damping properties (case i), with damping property only assigned to material elements (case ii), with damping property only assigned to CONN3D2 connections (case iii), and with damping property assigned to both material elements and CONN3D2 connections (case iv). All three cases i, ii and iii with $\alpha=-0.05$

have difficulty to converge at the beginning of simulation, therefore $\alpha=-0.41421$ is applied for these three cases. For case iv, no convergence issue with $\alpha=-0.05$, however similar case with $\alpha=-0.41421$ (case v) is applied for comparison purpose.

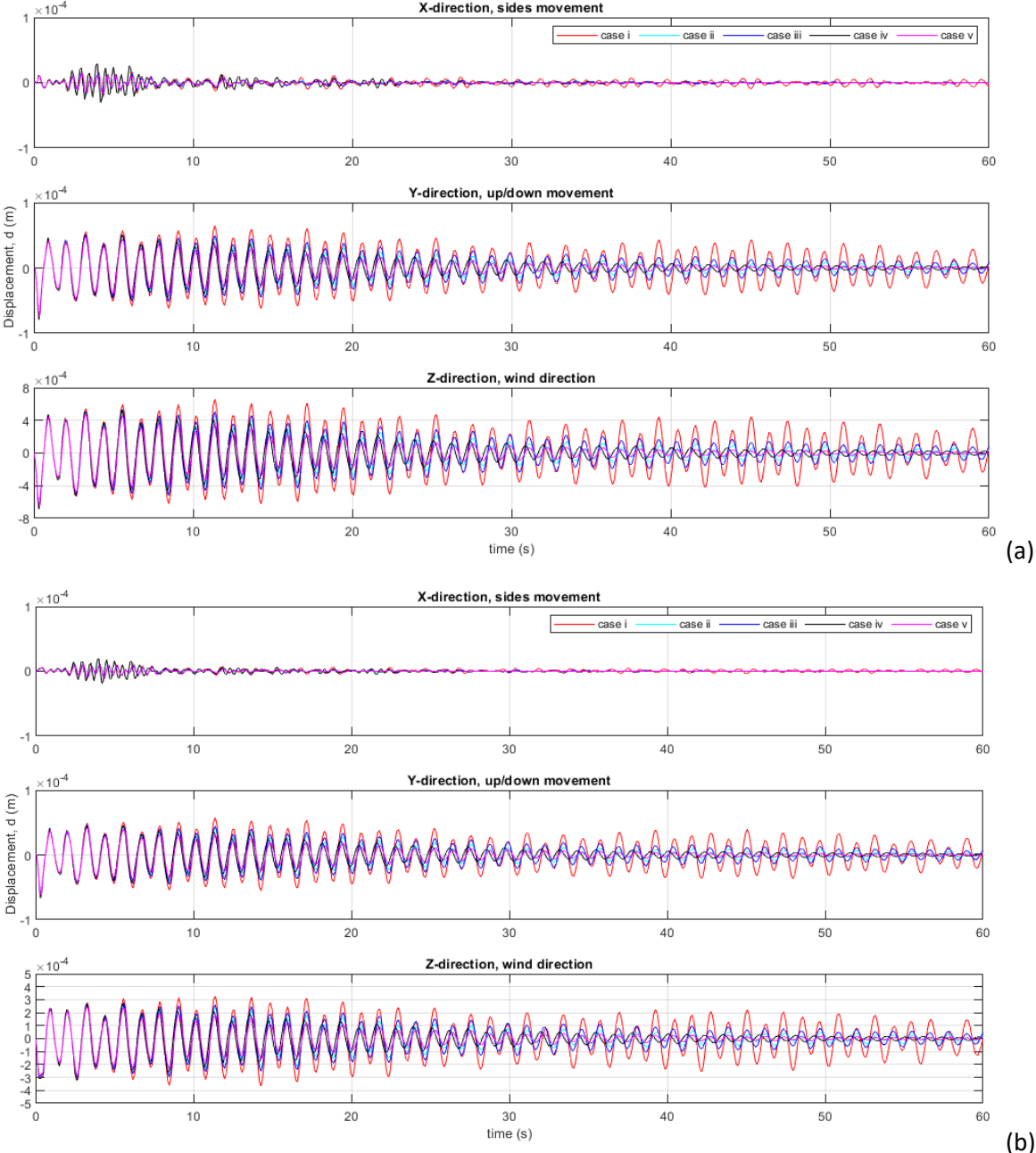


Figure 18 Results of sensitivity study with different damping settings, with numerical solution of in 60s, based on (a) rooftop and (b) 11th floor of the building

Table 6 Estimated δ and ξ

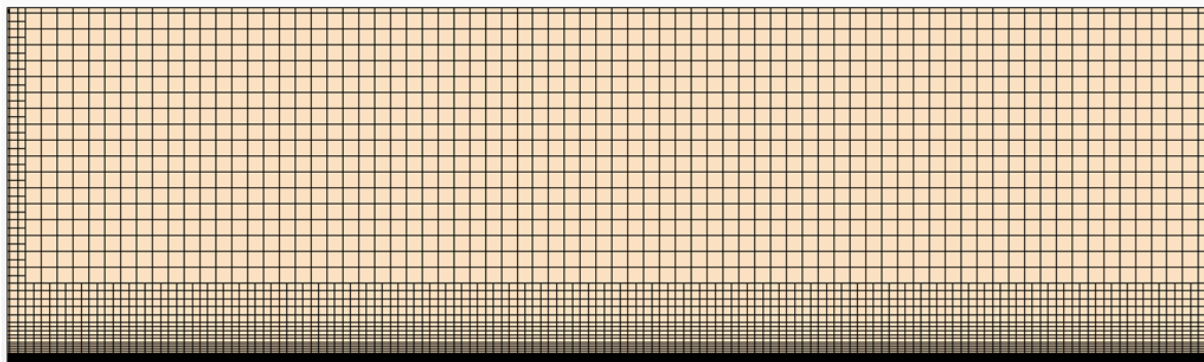
Case	Floor	Damping property	α -parameter	δ_s (%)	ξ_s (%)
i	Top	No	-0.41421	0.743	0.12
	11 th			1.504	0.24
ii	Top	Material		6.020	0.96
	11 th			6.536	1.04
iii	Top	CONN3D2		3.678	0.59
	11 th			4.420	0.70
iv	Top	Material+	-0.05	7.270	1.15
	11 th	CONN3D2		8.108	1.29
v	Top		-0.41421	7.783	1.24
	11 th			9.380	1.49

D. Preliminary testing on boundary conditions

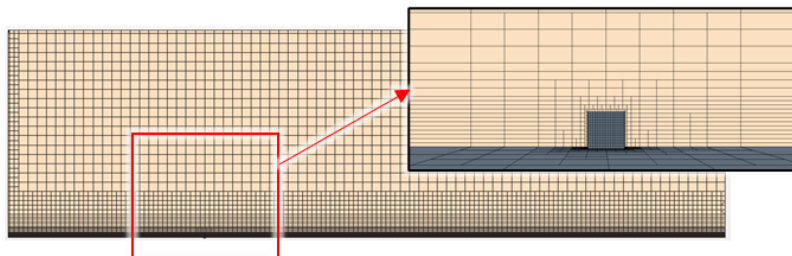
Preliminary testing of boundary conditions in ABL modelling are done on (i) an empty domain without building model, and (ii) a simple 6m x 6m x 6m (W x D x H) cubic block.

Similar dimension of CFD domain, i.e. 937m x 1757m x 510m (W x D x H) is used in all studies, and corresponding mesh profiles are shown in Figure 19. $y_0=0.01$ is applied in both tests, with near wall cell thickness $y_{g1}=0.712$ m. For inflow generation, $u_h=11.1\text{m}\cdot\text{s}^{-1}$ at $h=10$ m is applied in empty domain, and $u_h=10.13\text{m}\cdot\text{s}^{-1}$ at $h=10$ m [55] is applied for cubic block. Minimum 1000 iterations are applied to obtain the flow solution.

(a) Empty computation domain without building model



(b) Computation domain with 6m cubic block



(c) 6m cubic block

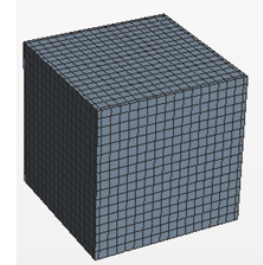
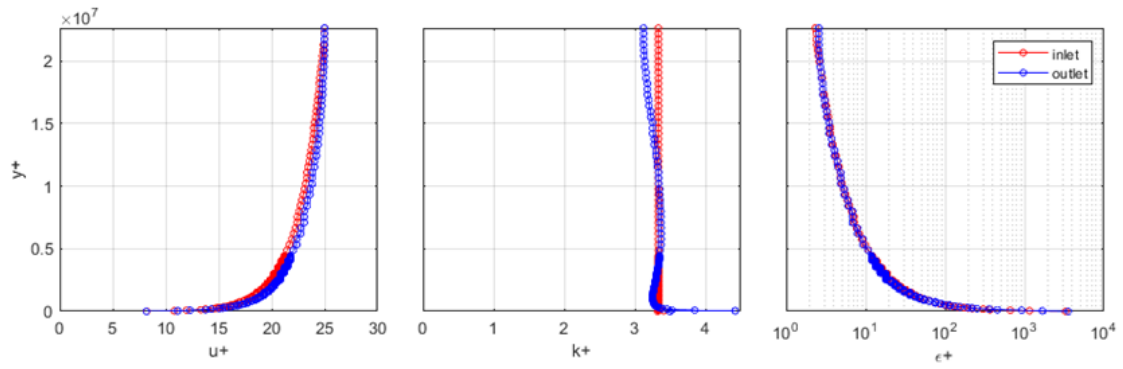


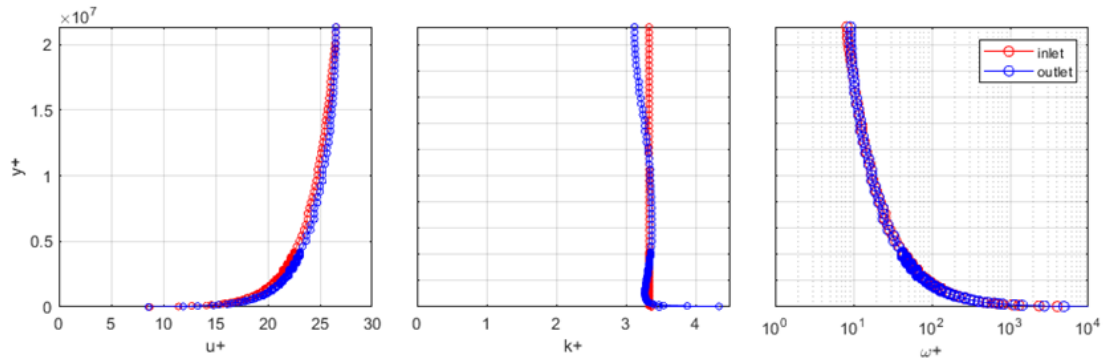
Figure 19 Mesh profile of (a) empty domain (b) domain with 6m cube (c) 6m cube

An initial test is done on an empty domain without building model using RN11-SKE, RN11-SSTKO, RN15-SKE and RN15-SSTKO models. Conservation of u , k , ϵ and ω profiles at inlet and outlet are compared. The u^+ , k^+ , ϵ^+ and ω^+ profiles against y^+ at inlet and outlet are shown in Figure 20. The shear driven RN11-SKE and RN11-SSTKO models maintain ϵ and ω profiles at inlet and outlet, while the pressure driven RN15-SKE and RN15-SSTKO models preserve u and k profile better across the domain. It is however observed that by applying Neumann BC at top boundary under RN11-SKE and RN11-SSTKO models, only slight improvements are obtained compared to using slip wall at top boundary, shown in Figure 21 with inflated x-axis. The BC used in this study has failed to replicate the results from Richards and Norris (2011) [31].

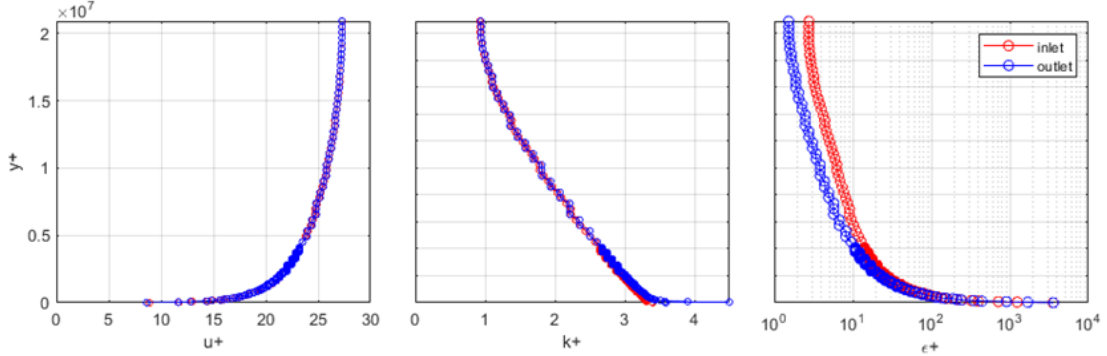
(a) RN15-SSTKO model



(b) RN15-SKE model



(c) RN11-SSTKO model



(d) RN11-SKE model

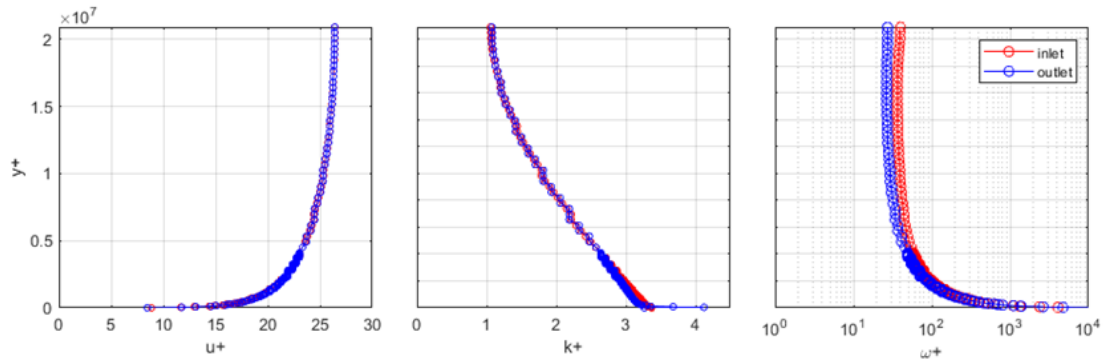


Figure 20 U^+ , k^+ , ϵ^+ and ω^+ profiles of (a) RN11-SKE, (b) RN11-SSTKO, (c) RN15-SKE, and (d) RN15-SSTKO

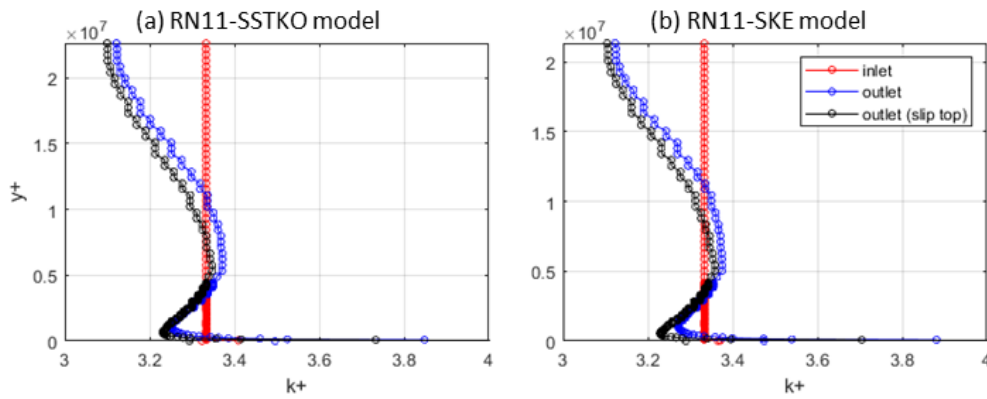


Figure 21 ϵ^+ profile using (a) RN11-SKE and (b) RN11-SSTKO, compared to if only slip wall applied to top boundary

The pressure coefficient C_p profiles of 6m cubic block under different BC models are shown in Figure 22 and Figure 23. The simulated results are compared against field measured data at Silsoe (denoted 'Silsoe'), wind-tunnel data of Wintechologische Gessellschaft (denoted 'WT') from Richards et al. [55], and an LES simulation result by Lim et al. [56]. Both SSTKO models show similar trends with the WT data. Compared to Silsoe data, parallel C_p value at windward and leeward walls are obtained, however significant deviation is observed at the roof façade for all four models. There are distinct C_p profiles between SKE and SSTKO models. The C_p profile on the roof using SSTKO models have comparable zones division given in EC1-4 [53] for flat roof type.

Profiles of μ_t/μ ratio and u^+ are presented in Figure 24 and Figure 25. Similar to pressure profile, there are distinct turbulence and velocity profiles between SKE and SSTKO models. It is observed that SSTKO models show better developed turbulence profiles especially on top of the roof.

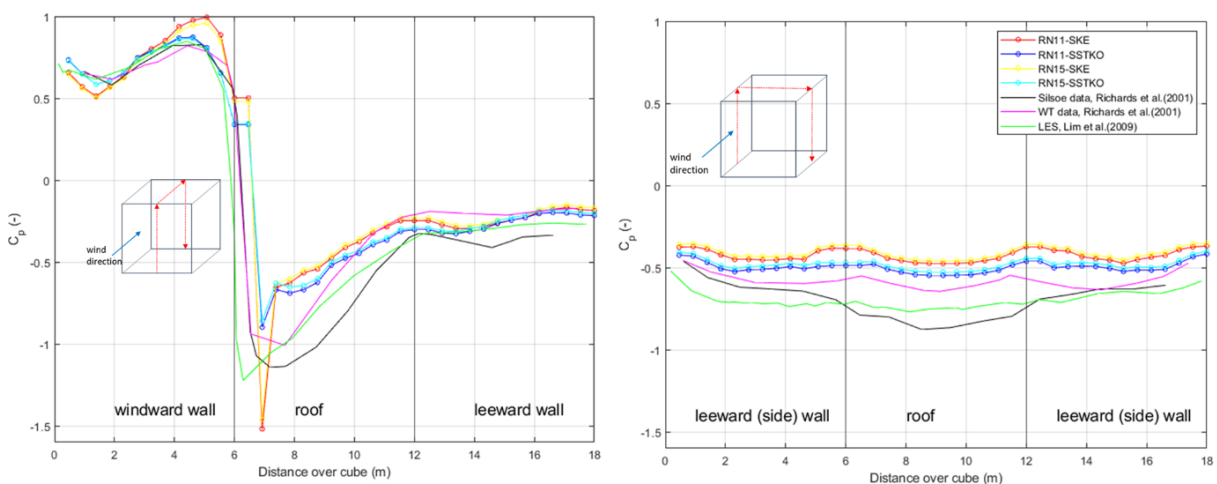


Figure 22 C_p profile of 6m cube

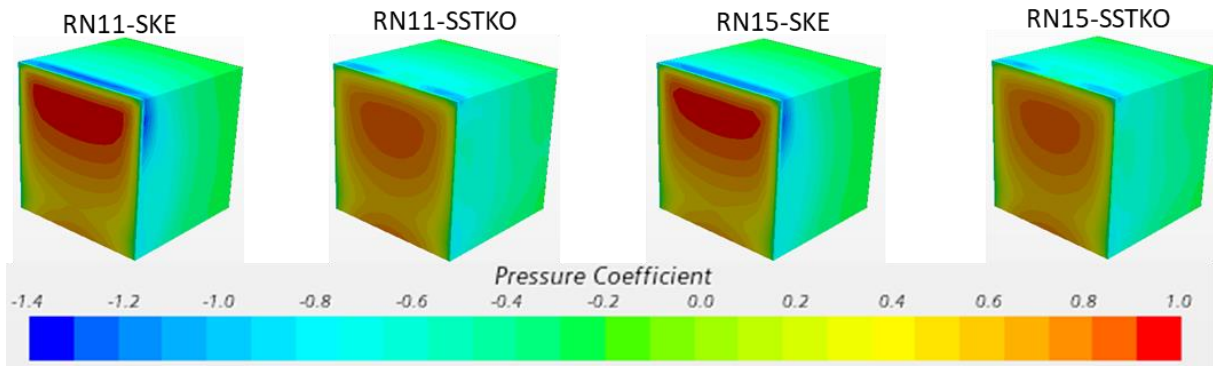


Figure 23 C_p profile of 6m cube domain

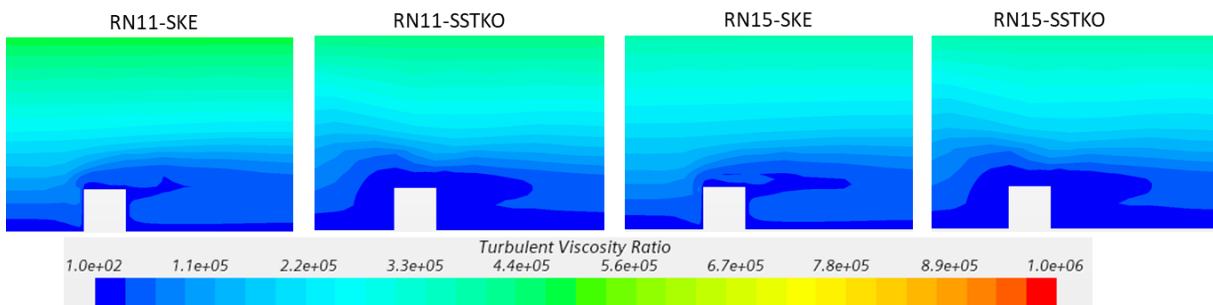


Figure 24 μ_t/μ ratio profile of 6m cube domain

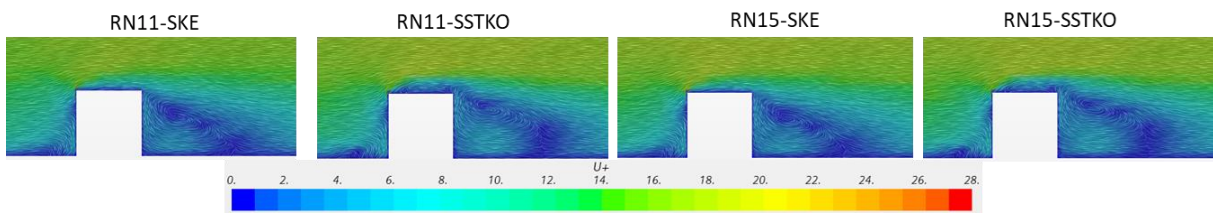
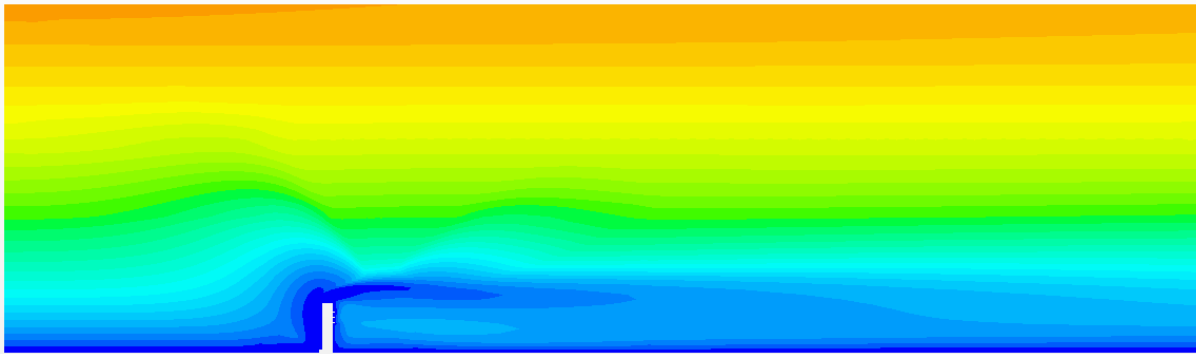
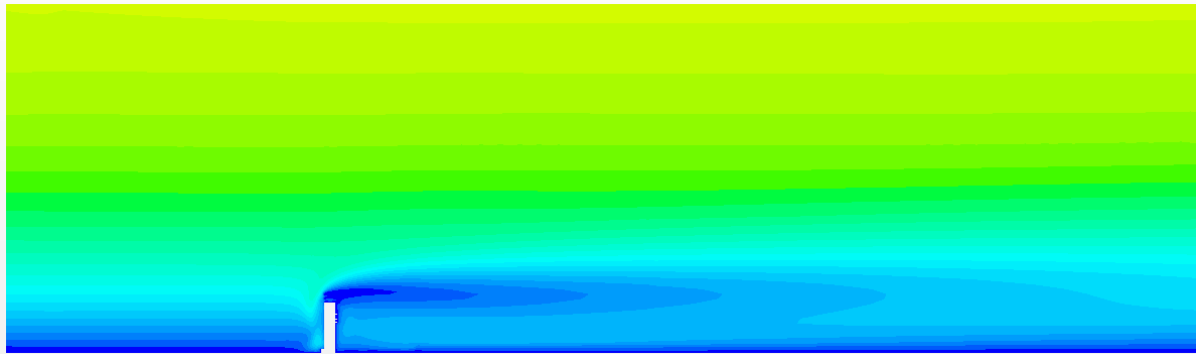


Figure 25 U^+ profile of 6m cube domain

E. Comparison between SKE and SSTKO models



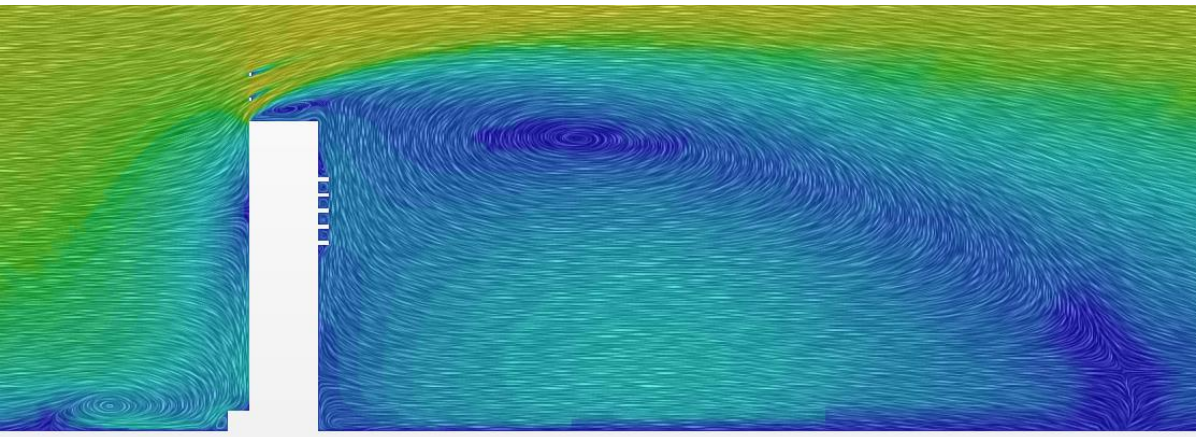
(a) RH15-SSTKO model



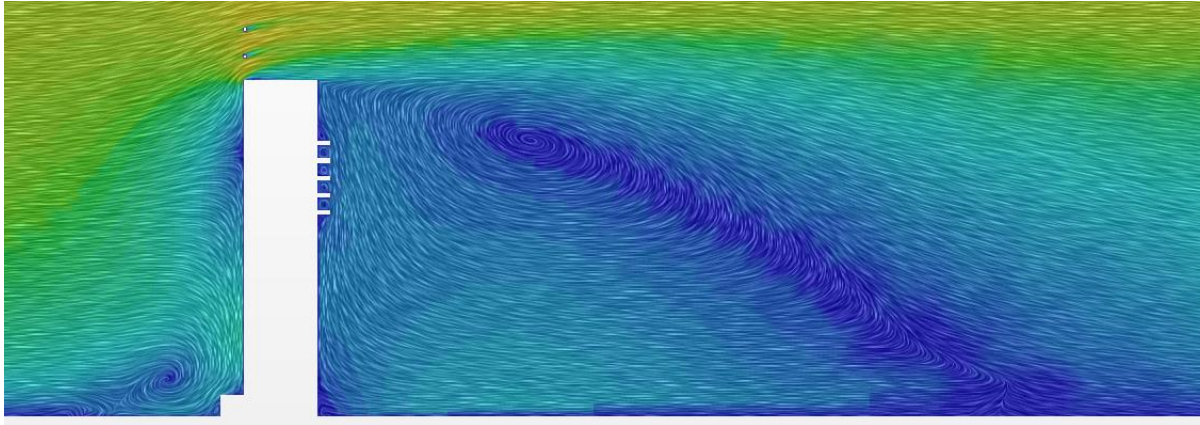
(b) RH15-SKE model



Figure 26 μ_t/μ ratio profile



(a) RH15-SSTKO model



(b) RH15-SKE model

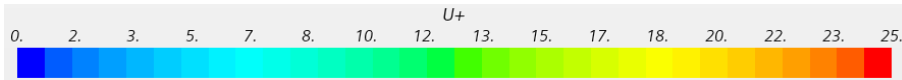
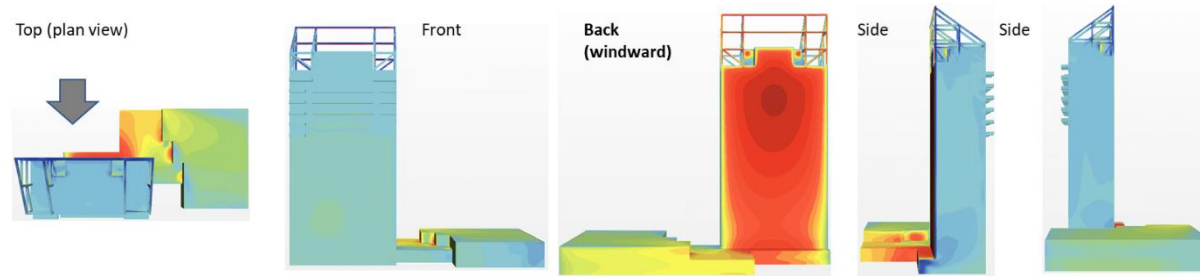
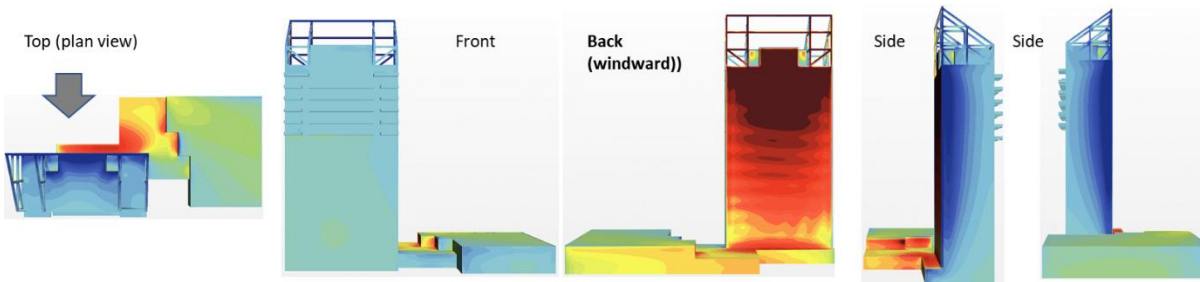


Figure 27 U_+ profile



(a) RH15-SSTKO model



(b) RH15-SKE model

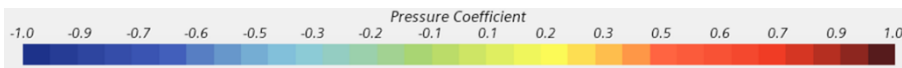


Figure 28 C_p profile

F. Testing with ideal gas model

In CWE, the atmospheric flow is assumed incompressible due to their relatively low speeds. Constant density model is therefore applied to the air flow, on the assumption that density is invariant throughout the domain. However under incompressible URANS solver, the propagation of air flow is instantaneous in the whole flow field at an infinite speed of sound, which may not be representative to a realistic atmospheric flow. While it is not commonly applied, an ideal gas model which allow mild compressible behaviour is included here to test their effect on the flow field, in comparison to the constant density gas model.

Under ideal gas law, the air density is a function of temperature and pressure. Isothermal model where temperature is assumed constant is applied in this test. Using this model, a mild compressible behaviour of field solution is expected. The flow domain is first initialized until flow solution are converged, using RH15-SSTKO BC settings, with segregated fluid isothermal model and ideal gas model. Once converged, unsteady simulation is run with the same wind speed for a total duration of 320s, using $\Delta t=1s$ with 5-20 inner iterations. This is followed by imposing a simple discrete change on u_h from $22.0m \cdot s^{-1}$ to $22.1m \cdot s^{-1}$ with a time step of $\Delta t=0.1s$ at 320s. In the second test, a similar ECG shape time-varying u_h profile with mean $22m \cdot s^{-1}$, time period of 5s and peak gust at $27m \cdot s^{-1}$ is imposed at inlet in the period of 320 and 325s.

The velocity profile at 10m from the ground are plotted in Figure 29. Similar to constant gas model, even if a time-independent velocity input is given, the flow under ideal gas model is oscillating at the upstream. It can be observed that their oscillating amplitudes are bigger than constant gas model under the same referenced speed. A substantial large oscillating pattern can also be found on the pressure profile as shown in Figure 30.

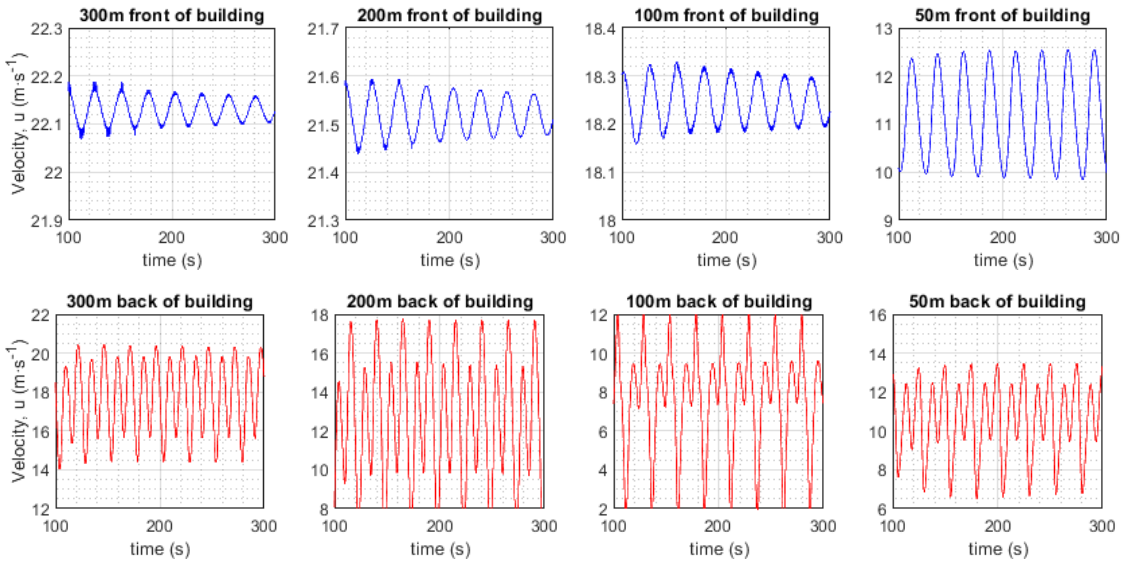


Figure 29 Velocity profile at selected probes of flow domain

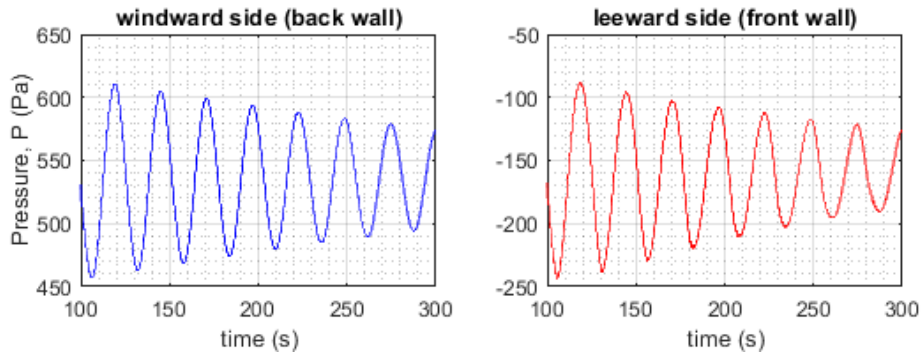


Figure 30 Pressure profile (maximum magnitude) at windward and leeward side of the walls

When applying a simple u_h variation from $22.0\text{m}\cdot\text{s}^{-1}$ to $22.1\text{m}\cdot\text{s}^{-1}$ at 320s, the velocity field does not update instantaneously in the entire domain, shown in Figure 31, which is different from their constant density model counterpart where an obvious ‘jump’ can be noticed in the whole domain. The upstream flow does react within a short time period after the change of inflow velocity. For building surface pressure, there is an obvious ‘jump’ on both windward and leeward walls after 1s of the change of inlet velocity, shown in Figure 32, with increment of 100Pa on both faces. Inconclusive trend can be deduced from this simple test.

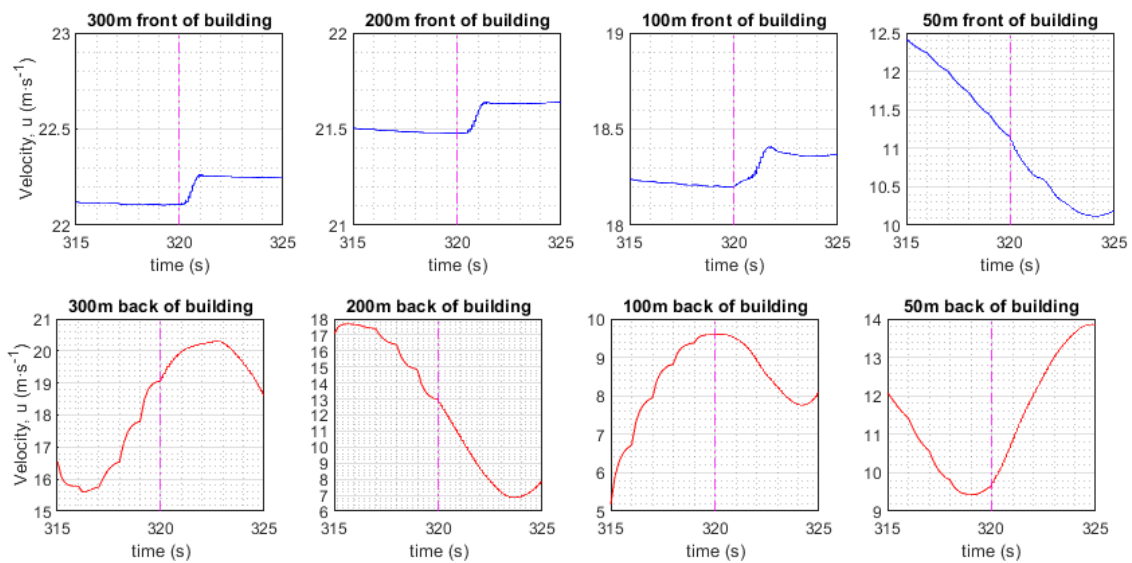


Figure 31 Selected velocity profile of flow domain at front and back of the building

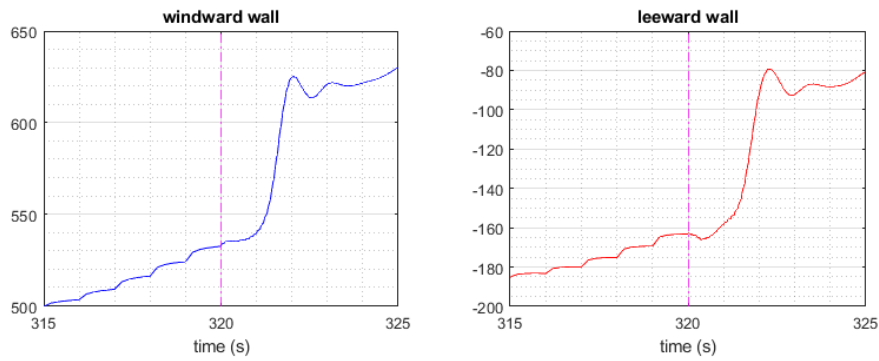


Figure 32 Pressure profile (maximum magnitude) at windward and leeward side of the walls

For second test with a ECG time-varying u_h profile, the change of velocity field is apparent in the upstream flow in response to the change at inlet velocity, while impact on downstream flow is less obvious but still noticeable, shown in Figure 33. Similarly, the building surface pressure taken from windward and leeward walls are responded to the change of inlet velocity, shown in Figure 34, though with a smaller magnitude compared to the constant gas model. It is however obvious that the fluctuation of both velocity and pressure fields persist for the remaining simulation, especially for the velocity at upstream and pressure field in the whole domain. This behaviour is the major difference in comparison to constant gas model, where in constant gas model the ‘big adjustment’ only happens during the change of inlet velocity and take a few more time steps to return to the solution close to steady state.

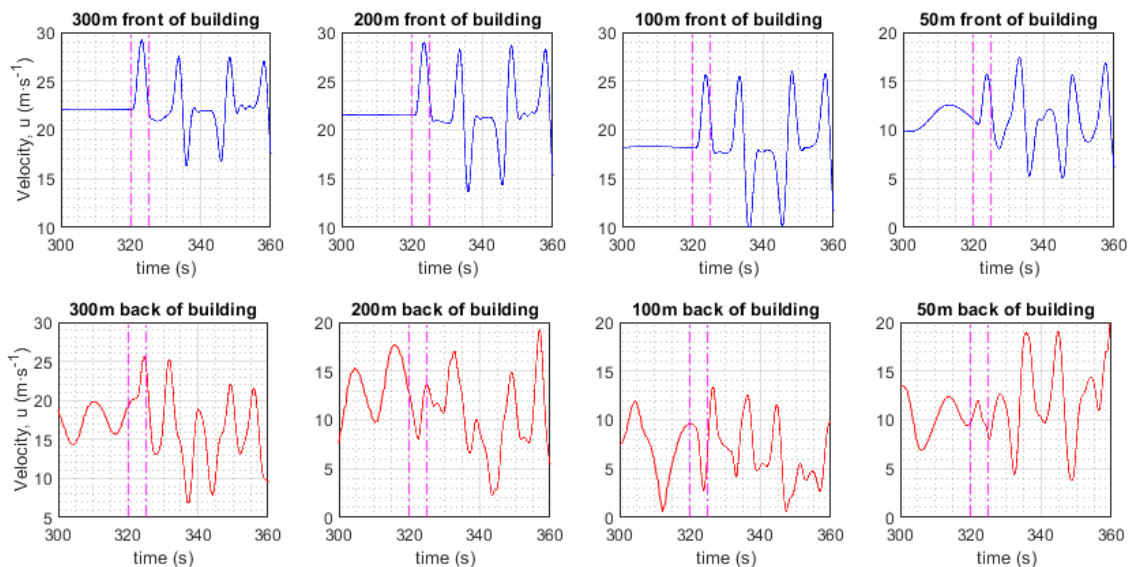


Figure 33 Velocity profile at selected probes of flow domain under ECG shape time-varying wind, using ideal gas model

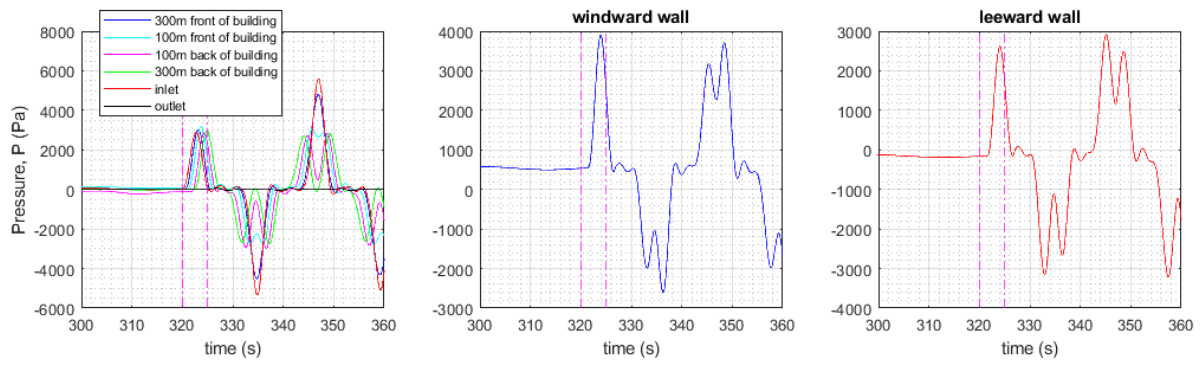


Figure 34 Pressure profile of selected probes and building surface under ECG shape time-varying wind, using ideal gas model

Based on the results obtained from above simulation, it is not recommended to use ideal gas model for ABL simulation.

G. Animations

Included as attachment:

1. Streamline and building surface pressure coefficient under constant wind speeds
2. Building displacement and building surface pressure under constant wind speeds
3. Vortex and building surface pressure under gust